GEORG-AUGUST-UNIVERSITÄT GÖTTINGEN IN PUBLICA COMMODA SEIT 1737

Fakultät für Physik [q,p]=iħ

Master's Thesis

Qualitätskontrollsysteme und Prozesse für die ITk Modul Produktion

Quality Control Systems and Processes for ITk Module Production

prepared by

Ruben Förster

from Münster

at the II. Physikalischen Institut

Thesis number:	II.Physik-UniGö-MSc-2026/01
Thesis period:	1st August 2025 until 31st January 2026
First referee:	Prof. Dr. Arnulf Quadt
Second referee:	Prof. Dr. Jörn Große-Knetter

Abstract

Der Atlas Inner Tracker (ITk) ist ein Halbleiter-basiertes Upgrade des Atlas Inner Detector im Rahmen des High Luminosity Lhc. ITk besteht aus verschiedenen Streifen und Pixel Detektor-Modul-Typen. Eines dieser Modultypen sind die ITk-Pixel-Quadmodule mit vier Auslesechips pro Modul. Für den Bau von ITk müssen über 10.000 solcher Quadmodule produziert und getestet werden. Diese Aufgabe wird von verschiedenen Produktionsstätten auf der ganzen Welt übernommen. Diese Masterarbeit beschreibt Maßnahmen, die ergriffen wurden, um die in Göttingen durchgeführten Produktionsschritte zu optimieren. Im besonderen Fokus liegen das Design, der Bau und die Inbetriebnahme eines Teststandes für die elektrische Qualitätskontrolle der Module.
Zusätzlich wird eine Studie zur Erforschung der Auswirkung thermischer Zyklen in Bezug auf Core-Column-Probleme, ein häufig auftretendes Problem der Module, durchgeführt. Diese Studie dient dem Zweck, sicherzustellen, dass die Module die Umgebungsbedingungen während ihrer Betriebszeit im Detektor überstehen können.

Abstract

The Atlas Inner Tracker (ITk) is an all silicon upgrade to the Inner Detector of Atlas in the context of the High Luminosity Lhc. ITk consists of different types of pixel and strip subdetector modules. ITk Pixel quad modules are such a type of module and include four readout chips. Over 10,000 quad modules need to be produced and tested. This task is spread out over multiple production sites across the globe. This master's thesis describes steps undertaken to optimise the production and testing stages performed in Göttingen. A special focus is put on the design, construction and commissioning of a new setup for electrical testing of the modules.
Additionally, a study to understand the effects of thermal cycles on the modules with respect to so-called Core Column issues is performed. Core Column issues are a common problem encountered during the Quality Control testing of modules. This study is required to ensure modules are able to withstand the environmental conditions encountered over the lifetime of the detector.

Contents

1. Introduction

Today our physical understanding of the world around us has reached unprecedented levels in all fields of research. At the forefront of particle physics is the Standard Model (SM), which answers one of the most fundamental questions of science: What are we and the universe around us made out of?

The SM describes everything we can observe as being composed of 12 fermions, which make up all matter, and 3 fundamental forces, which are propagated by bosons, of which there are 5. These 17 elementary particles can be seen in Figure 1.1. Although their properties can describe nearly all phenomena found in the universe, open questions remain. This includes the search for exotic matter, as well as fundamental questions about the early universe, including the unification of forces at high energy densities and understanding the cause of CP violation in the early universe.

Experimental data forms the foundation of our understanding of the universe and is the key to finding answers to open questions in physics. At the forefront of experimental particle physics are large-scale experiments located at particle accelerators, which enable the collision of matter at energies high enough to cause hard scattering between particles, breaking them into their fundamental constituents, the elementary particles. This enables one to understand their properties and types of interactions by measuring the remnants coming from the collision point with large detector experiments.

The largest accelerator currently in operation is the Large Hadron Collider (LHC) at CERN [1], which allows for collisions at centre of mass energies of 13.6 TeV. To increase its capabilities even further, the LHC will undergo a major upgrade starting in 2026. The High Luminosity Upgrade will increase the amount of data collected from the 4 large experiments at the LHC by an order of magnitude [2]. This will allow the study of types of interactions and events that are incredibly rare and will therefore open up potentially new frontiers to discover physics beyond the Standard Model (BSM).

One of the detector experiments at the LHC is the ATLAS experiment. To handle the increased track densities and increased radiation load at the centre of ATLAS, an all-new inner detector is being built: The ATLAS Inner Tracker (ITk) [3]. ITk will be made up of thousands of small detector modules. One type of modules is the ITk Pixel quad

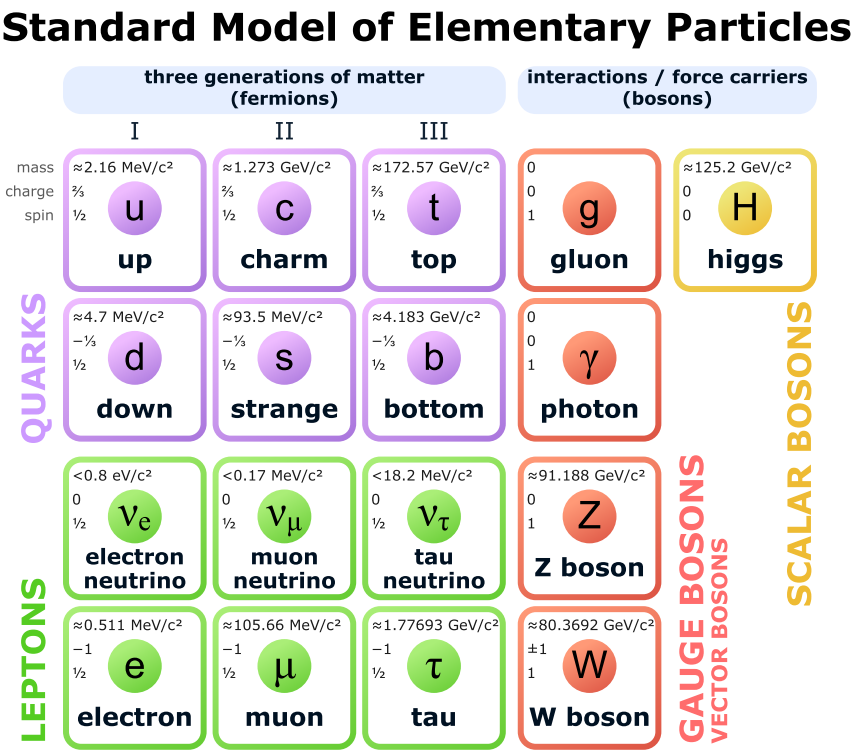

Figure 1.1.: The Standard model [1].

module of which over 10,000 are being produced. The construction of these modules is an effort spread across many research sites all around the world, including the production of 1,800 modules in the German Outer Barrel Cluster. Each module placed in the final detector must achieve a set of quality standards. Quality Control (QC) testing is therefore imperative.

To ensure time-efficient production that stays on schedule while also ensuring quality, reliable testing setups and optimised lab processes are essential to the ITk project.

[1] Image by MissMJ (Modified), CC BY 3.0, https://commons.wikimedia.org/wiki/File:Standard_Model_of_Elementary_Particles.svg

2. The Large Hadron Collider & ATLAS Experiment

The Large Hadron Collider (LHC) at the European Organisation for Nuclear Research (CERN) in Geneva is the largest collider of its kind [1]. Made possible by the international collaboration between 25 member states and thousands of physicists, and located in a 26.7 km long circular underground tunnel, it allows collisions of particles with energies up to 13.6 TeV. While this tunnel previously housed the Large Electron-Positron Collider (LEP), as the name suggests, the LHC accelerates hadrons, specifically protons and heavy ions. It allows the study of the fundamental building blocks of our universe, enabling major discoveries, most notably the discovery of the Higgs boson in 2012 [4].
The accelerator complex located at CERN is shown in Figure 2.1. While the LHC is the largest accelerator at CERN, it can be seen that it is far from the only one. Smaller accelerator rings like the SPS and PS serve many smaller experiments or as preaccelerators to the LHC, where particles are brought up to sufficient energies before being injected into the next larger ring.
The LHC itself collides particles at rates up to 40 MHz at 4 collision points where it hosts 4 large experiments: ALICE, LHCb, CMS, and ATLAS [1].

ALICE (A Large Ion Collider Experiment) is targeted at studying heavy ion collisions, such as Lead-Lead collisions, which form a quark-gluon-plasma and further our understanding of the early universe [5].

LHCb focuses on B-hadron physics and is aiming to further our understanding of CP violation [6].

CMS & ATLAS are both general-purpose detectors, studying a wide range of phenomena, probing parameters and predictions of the Standard Model and looking for potential evidence of physics beyond the Standard Model (BSM) [7, 8]. Both detectors are built around a collision point covering nearly all spatial directions, meaning that particles coming from the collision point at the centre of these detectors will pass through the detectors

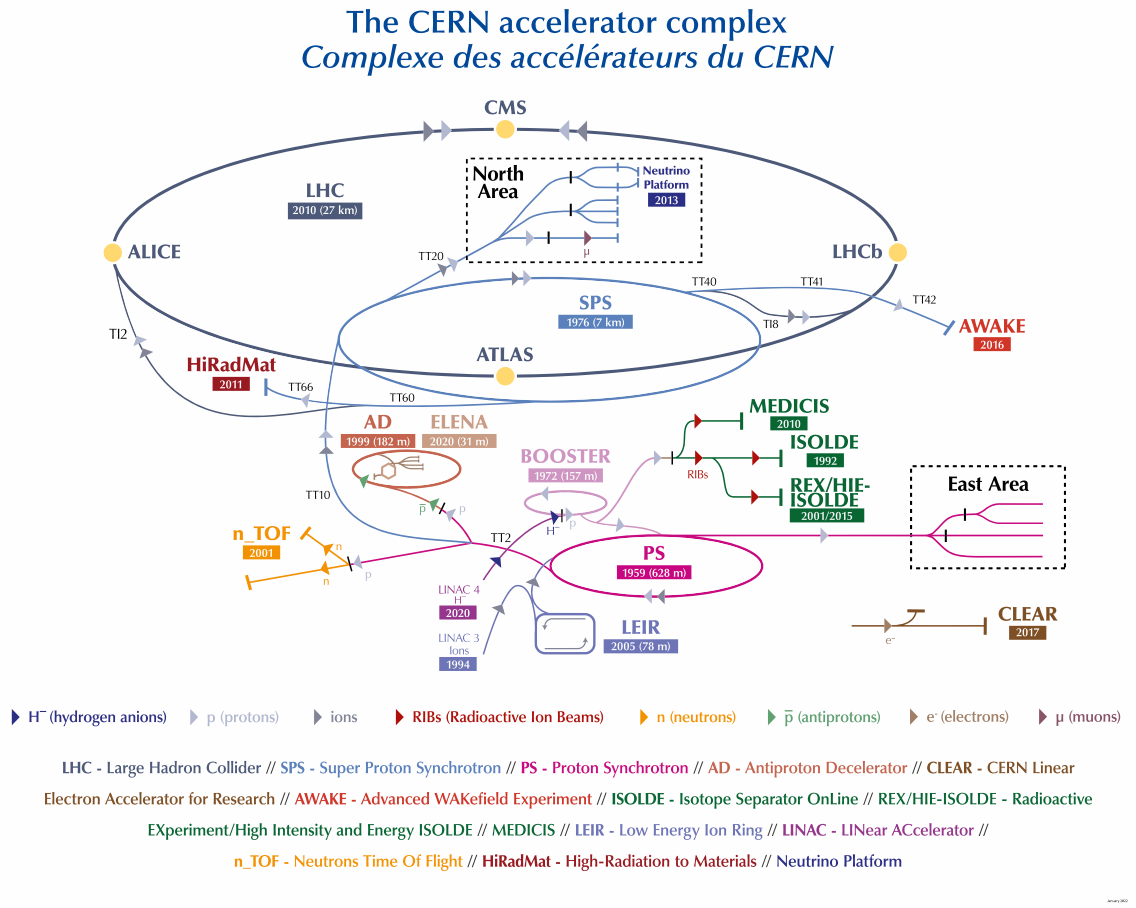

Figure 2.1.: Accelerator complex at CERN. ©CERN

no matter in what direction they go into. The following thesis will focus on ATLAS, and its upgrade as part of the High Luminosity LHC.

2.1. The Atlas Experiment

The ATLAS experiment (Figure 2.2) is located at Point 1 of the LHC and is the largest experiment by volume [7]. It consists of a system of magnets and multiple subdetectors working together to identify and track particles coming from the collision point at the centre of the detector. This enables the reconstruction of events happening at the collision point.

The detector needs to handle extremely high collision rates of 40 MHz [1], which creates challenges both in the readout speed as well as the radiation hardness of the electrical components used. Additionally, the detector aims to achieve a large angular coverage close to 4π. This is especially relevant in regions close to the beam pipe. For this reason,

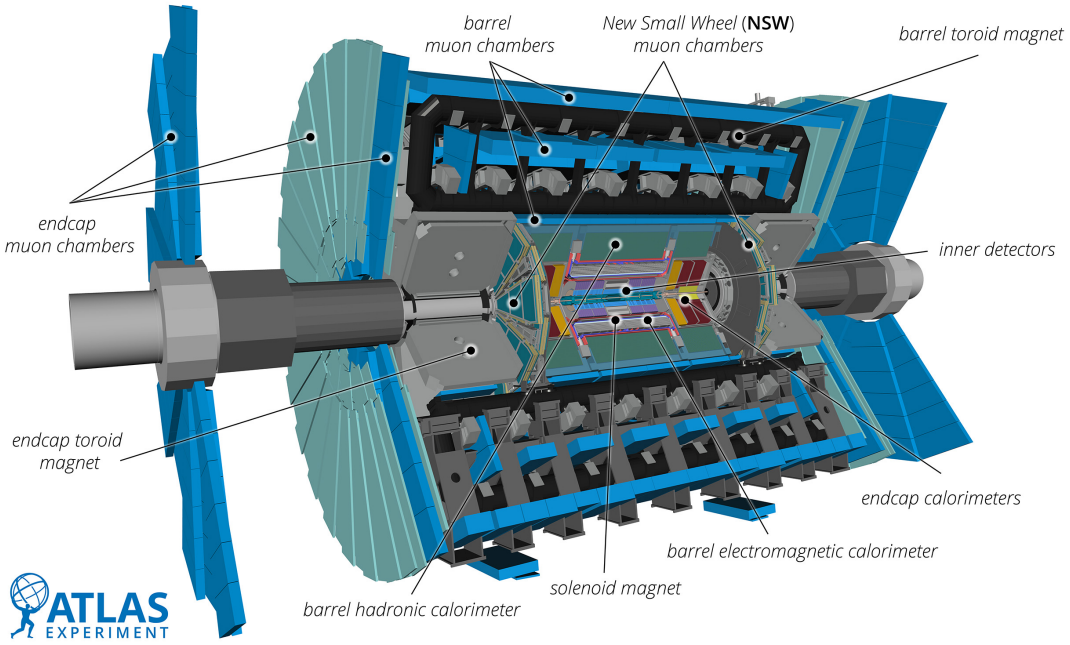

Figure 2.2.: Cutaway view of the Atlas experiment. ©Cern

Atlas is built in a cylindrical design with most subdetectors consisting of a barrel section as well as end caps covering angles closer to the beam pipe in the forward and backward directions. The coverage is expressed as a region of pseudorapidity $|\eta|$, where larger $|\eta|$ values correspond to shallower polar angles closer to the beam pipe.
The subsequent section is a description of Atlas as of the beginning of 2026 and is then expanded upon in Section 2.2, discussing changes and upgrades to Atlas as part of the High Luminosity Lhc (HL-LHC).

Inner Detectors

The Inner Detector (ID) of Atlas includes the Pixel, Silicon Microstrip Tracker (SCT) and Transition Radiation Tracker (TRT), as well as the Insertable B-Layer (IBL) added during the first long shutdown of the Lhc [9]. These tracking detectors work together to identify the exact path (i.e. track) a particle takes in all dimensions. Due to their location close to the beam pipe, these subdetectors have to withstand and identify the highest particle flux.

The Pixel Detector is located closest to the beam pipe and originally consisted of 3 layers, with approximately 80.4 million readout channels in total [10]. It is a Silicon Pixel Detector, as described in Section 3.4 and covers a region of $|\eta| < 2.5$.

The IBL was installed in 2014 [9]. It is an additional innermost layer of the Pixel Detector. It surrounds the beam pipe tightly, consists of 14 Carbon staves and was designed to survive a total integrated luminosity of 300 fb^{-1}, allowing ATLAS to maintain and improve its performance during its operation.

The SCT is positioned outside the Pixel Detector and is made of 8 layers of Silicon Strip Detectors as described in Section 3.4. It also covers a region of $|\eta| < 2.5$. The mean pitch of strips is approximately 80 µm [11].

The TRT is a type of gas-filled detector consisting of 300,000 so-called straws. This architecture allows particles to have many detection points used for momentum measurements [12]. It covers regions up to $|\eta| = 2.0$. The functionality of gas filled detectors is described in Section 3.2. Additionally, transition radiation is created depending on the particle velocity when passing through materials with different refractive indices [12]. This allows for particle identification by differentiating between particles with different masses.

Calorimeters

ATLAS's sampling calorimeters cover a range of $|\eta| < 4.9$ and are located outside the tracking detectors [7]. The functionality of calorimeters is explained in Section 3.3. Their purpose is the measurement of the energy of incoming particles. The ATLAS calorimeters consist of a Liquid Argon (LAr) electromagnetic calorimeter and hadronic calorimeters. Like all other ATLAS detectors, the calorimeters are also divided into a barrel and end cap sections. It is critical for their functionality as well as the functionality of the muon system that electromagnetic and hadronic showers are contained within the calorimeters.

Muon Spectrometer

The muon spectrometer is positioned outside of the calorimeters and is optimised for muon identification. It consists of monitored drift tubes and multiwire proportional chambers (MWPCs) [13], which are both types of gas filled detectors described in Section 3.2. The barrel of the muon spectrometer consists of 3 stations which measure the position of muons with a precision of 50 µm. The end cap consists of 3 disk-shaped measuring stations called wheels, which also have a resolution of 50 µm.

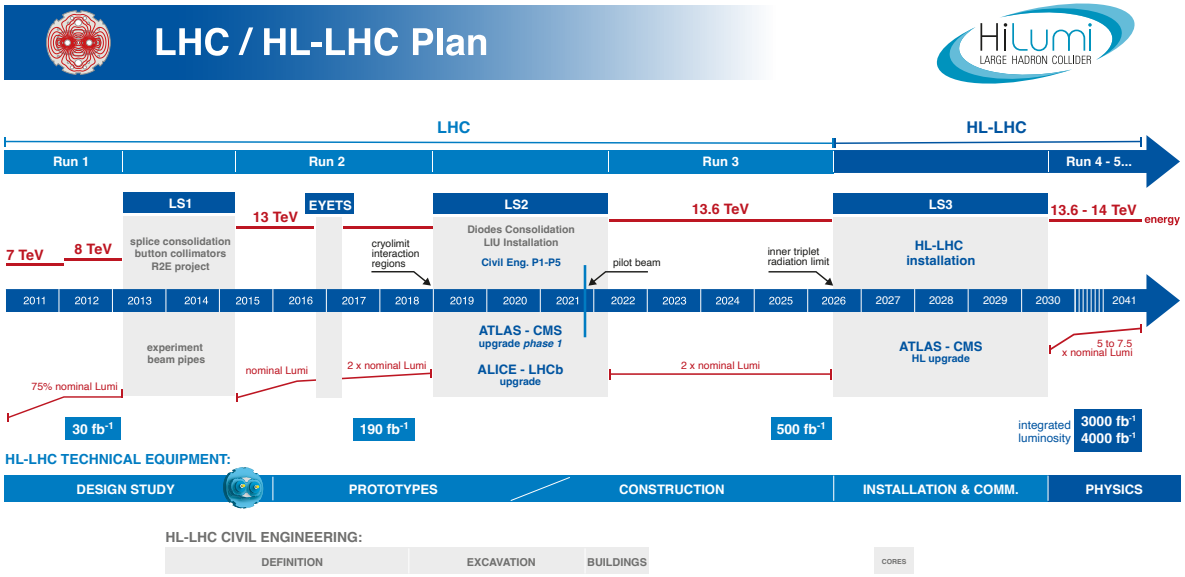

Figure 2.3.: Timeline of LHC operations and the High Luminosity upgrade. ©CERN

Magnet System

Determining the momentum and charge of a particle is achieved by applying a magnetic field and measuring the curvature of the resulting track inside the previously introduced detectors. The ATLAS experiment, therefore, is equipped with large superconducting magnets. There are 2 main systems. The toroid magnets provide a magnetic field of 0.5 to 1 T to the muon spectrometer, while the inner detectors lie within a 2 T homogenous magnetic field provided by a solenoid magnet [14].

2.2. The High Luminosity LHC

For a given process of scientific interest with the cross-section σ, the number of events that occur over the measurement duration can be described as [15]

$$N = \sigma \int \mathcal{L}(t)dt \tag{2.1}$$

With $\mathcal{L}$ being the instantaneous luminosity. The integrated luminosity $\int \mathcal{L}(t)dt$ can therefore be thought of as a measure of the amount of data from collisions recorded over a given time period. Increasing the luminosity of the LHC, therefore, will enable the study of rare events with low cross-sections. The coming upgrade to the LHC, named High Luminosity LHC (HL-LHC), will do precisely this. The installation of this upgrade will take

place during the Long Shutdown 3 (LS3) between 2026 and 2030 and will increase the instantaneous luminosity approximately by a factor of 10 to $5 \times 10^{34}\,\mathrm{cm}^{-2}\mathrm{s}^{-1}$ and the integrated luminosity by 10 [2]. This is achieved by increasing the number of collisions per bunch crossing (pileup) to up to an average of 200 while keeping the collision rate fixed at 40 MHz. Additionally, the centre of mass energy is expected to be increased from $\sqrt{s} = 13.6\,\mathrm{TeV}$ to 14 TeV [2]. A timeline of the HL-LHC upgrade plan can be seen in Figure 2.3.

The increased pileup creates significant challenges for the ATLAS experiment, which needs to handle both an increase in radiation while also having to detect and process the significantly higher particle flux and associated data rates. Additionally, precision tracking will become even more relevant with the increased pileup since the reconstruction of particle tracks needs to be precise enough to allow vertexing of the individual interaction points. The ATLAS experiment will therefore undergo upgrades to many of its systems and subdetectors [2]. The calorimeters will undergo an upgrade of their detector electronics and the muon spectrometer will see the upgrade of chambers for their inner layers. The trigger and Data Acquisition (DAQ) system will need to be upgraded to handle the increased data rate of 5 TB/s [16]. The most significant upgrade will be the complete replacement of the Inner Detector by the ATLAS Inner Tracker (ITk), which is the focus of this thesis and will be further detailed in Chapter 4.

3. Particle Detectors

Particle detectors find a wide variety of applications, including personal safety, medicine and power generation[1]. The following chapter will focus in particular on particle detectors within Particle Physics and collider experiments, although many of the described principles might apply to other applications as well. All detectors fundamentally use the interaction of particles with a detector medium. While historically, the methods for recording these interactions have also been more manual, modern particle detectors almost exclusively record these effects by converting the interaction into electrical or optical signals, which are then digitised. This makes it possible to create large detectors with many readout channels operating at extremely high data rates.

3.1. Interaction of Particles with Matter

When a particle passes through a detector medium or any other type of matter, it can interact in different ways. The type of interaction depends on the type of particle, its energy and the material it is passing through. This typically results in the creation of charged particles through phenomena like ionisation, or the creation of photons in processes like bremsstrahlung. The following chapters will cover different (although by far not all) ways to describe these interactions between particles and matter. Understanding them is not only necessary for understanding the functionality of particle detectors but also for applications like radiation shielding and safety.

Photons

Photons passing through material can be described by 3 major effects, which can be seen in Figure 3.1: The photoelectric effect, the Compton effect and pair creation.

The photoelectric effect [18] describes the interaction of a photon with an electron in the shell of an atom in the material. The photon gives its full energy to the electron,

[1] The content of the following Chapter 3 and its Subsections is largely based on [17], unless noted otherwise.

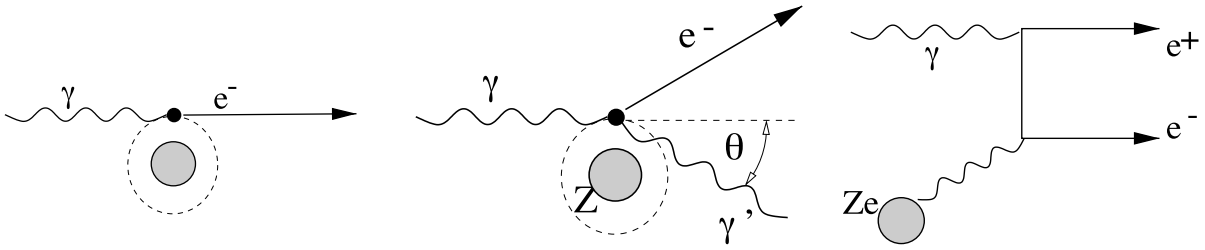

(a) Photo electric effect (b) Compton Scattering (c) Pair Creation

Figure 3.1.: Schematics showing different interaction types of photons with matter[2].

therefore ceasing to exist and ionising the atom. The cross-section of the photoelectric effect can be described as being roughly proportional to $\sim E^{-3.5} \cdot Z^5$, with E being the energy of the photon and Z the atomic number of the medium. It can therefore be seen that this effect dominates for high Z materials and low particle energies below 10 keV.

Compton Scattering [19] describes the scattering of a photon on an electron of the outer shell of an atom. The atom is ionised while the photon is deflected with an angle θ. Compton scattering dominates in regions of several keV up to 1 MeV and is proportional to Z.

Pair creation is the creation of an electron-positron pair, converting the mass of the photon into the mass and momentum of the new particles. This effect only occurs in a medium since the interaction is forbidden in a vacuum due to conservation laws that dictate that some momentum be transferred. The photon additionally needs an energy of at least the rest mass of the created particle pair, so pair creation is only possible above $E_\gamma > 2m_e = 1.022\,\text{MeV}$.

Charged Particles

Heavy Charged Particles

The interaction of heavy charged particles with matter can be described using the Bethe-Bloch Formula [20]. Heavy charged particles in this context include all particles except electrons and positrons. The Bethe-Bloch Formula describes the energy loss of a particle per unit path length:

$$-\left\langle \frac{dE}{dx} \right\rangle = K \frac{Z}{A} \rho \frac{z^2}{\beta^2} \left[\tfrac{1}{2} \ln\!\left(\frac{2\, m_e c^2\, \beta^2 \gamma^2\, T_{\max}}{I^2} \right) - \beta^2 - \frac{\delta(\beta\gamma)}{2} \right] \tag{3.1}$$

[2]Image Source: Kolanoski, Wermes 2015 [17]

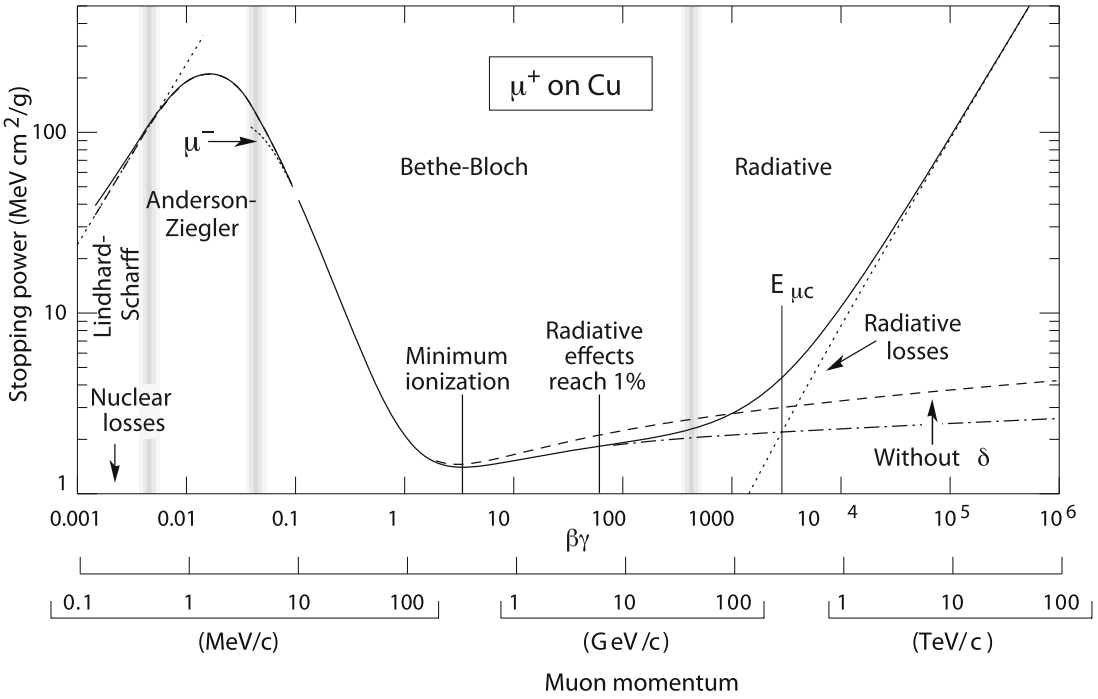

Figure 3.2.: Stopping power of μ^+ in Copper at different $\beta\gamma$[3].

K: 0.307 MeV cm^2/mol, z: particle charge, β: velocity, Z: atomic number, A: mass number, I: mean ionisation energy, $T_{\max}$: max. energy transfer, δ: density correction

It assumes an independent stochastic process for each particle interacting with individual atoms of the material. For low energies, a dependency of $1/\beta^2$ can be seen (Figure 3.2), while for large energies, kinematic and relativistic terms lead to a limited increase again. Overall, this forms a region of low stopping power at $\beta\gamma \approx 3 - 4$. Particles with this energy are also called Minimum Ionising Particle (MIP) [17].

Electrons & Positrons

Due to their low mass, both ionising effects and radiative effects need to be considered for electrons. Ionising effects also differ due to kinematic and spin effects. For positrons, additional antiparticle characteristics, such as annihilation, need to be considered.

Radiative Losses

At $\beta\gamma \gtrsim 100$, especially for electrons and positrons, effects caused by bremsstrahlung need to be considered. These effects are mainly caused by the interaction between the particle and the Coulomb field of the nuclei of an atom, leading to the emission of a photon. The

[3]Image Source: Kolanoski, Wermes 2015 [17]

energy loss due to these radiative effects is mainly dependent on the energy of the particle E and the atomic number Z and mass number A of the material [17]:

$$-\left(\frac{dE}{dx}\right)_{\text{rad}} \sim \frac{Z^2}{A}E \tag{3.2}$$

3.2. Gaseous Detectors

Gaseous detectors can be built in many designs. All these designs share the common feature of a detection volume filled with a noble gas mixture (for example Argon + CO_2) with an anode and a cathode. At their core is the principle of gas amplification [21]. Following the ionisation of gas atoms inside the detector, the charges are separated by the electric field between anode and cathode. The acceleration of the electron creates secondary ionisations, leading to an avalanche amplifying the primary charge. Different types of gaseous detectors feature different arrangements of anodes and cathodes that will, in turn, lead to different spatial and timing performance. Common types include Multi-wire Proportional Chambers (MWPCs), Drift Chambers or Time Projection Chambers (TPCs) [17].

3.3. Calorimeters

Calorimeters rely on the creation of particle showers inside their detector volume to determine the energy of the incoming particle. In contrast to tracking detectors, this process is destructive for the particle being measured. One can differentiate between two major types of calorimeters: electromagnetic and hadronic calorimeters.

Electromagnetic (EM) Calorimeters measure the energy of electrons, positrons, and photons, through the processes of bremsstrahlung and pair creation. A back and forth between these interactions leads to an electromagnetic shower composed of many particles. It can be shown that the size of the shower is proportional to the logarithm of the energy of the initial particle. The energy can therefore also be determined by measuring the signal created by the shower.

Hadronic Calorimeters detect high-energy hadrons by measuring their interaction with the atomic core of the atoms in a dense material. Inelastic scattering causes secondary particles, which, in case they have enough energy, will again interact with further atoms, creating a hadronic shower. The hadronic shower is significantly larger compared

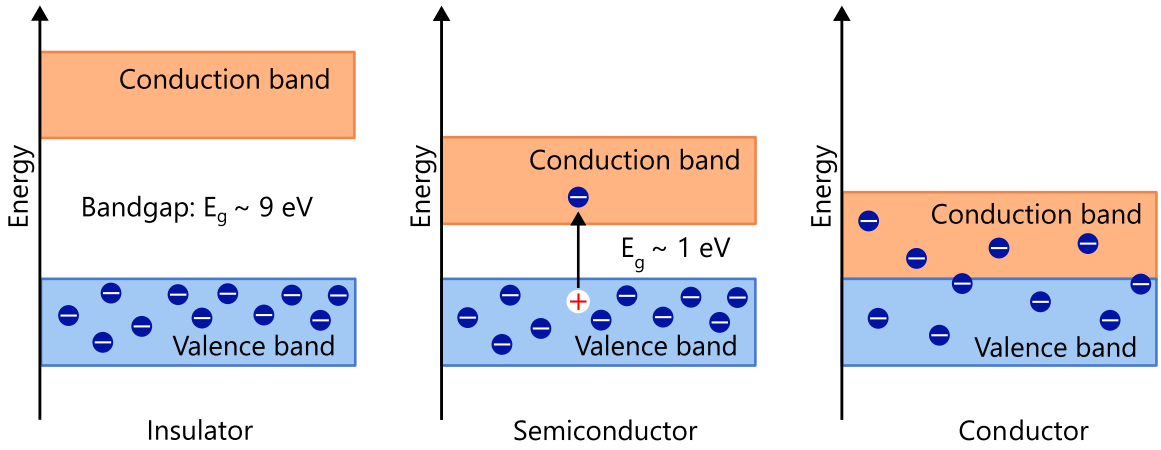

Figure 3.3.: Band gap of Insulators, Semiconductors, and Conductors[4].

to electromagnetic showers and will contain secondary EM showers through $\pi^0 \rightarrow \gamma\gamma$ decays.

3.4. Silicon Detectors

Silicon detectors use semiconductor technology to detect particles. At the core of Silicon detectors (and semiconductor technology as a whole) stands the PN-junction, which is made possible by doping a semiconductor material like Silicon.

Semiconductor Materials

Solid crystalline structures can be classified as conductors (metals), insulators, or semiconductors depending on the band structure of the material.
The band structure is formed by the densely packed periodic lattice of the atoms, influencing and splitting the energy levels of the respective atoms so often that nearly continuous regions are formed, which are then called bands.
For insulators, the two uppermost bands, called the valence and conduction bands, are separated by ∼9 eV, forming a band gap [17]. The conduction band lies far above the Fermi Level energy, allowing no free movement of charge. In conductors, the valence band overlaps with the conduction band, no band gap is present, allowing the free movement of electrons within the metal. Semiconductors such as Silicon or Germanium possess a small band gap of ∼1 eV [17]. This band gap can be overcome, causing an electron to move from the valence band to the conduction band and leaving behind a so-called hole, which can be treated as a positively charged particle.

[4]Image inspired by [22]

PN-junctions

The properties of semiconductors can be further altered by inserting atoms with one more or one fewer electron in their outer shell into the lattice structure [23]. This process is called doping and can be achieved by a multitude of processes, such as ion implantation or diffusion. This then leads to either an increase of electrons (n-doped) or an increase of holes (p-doped) acting as charge carriers.

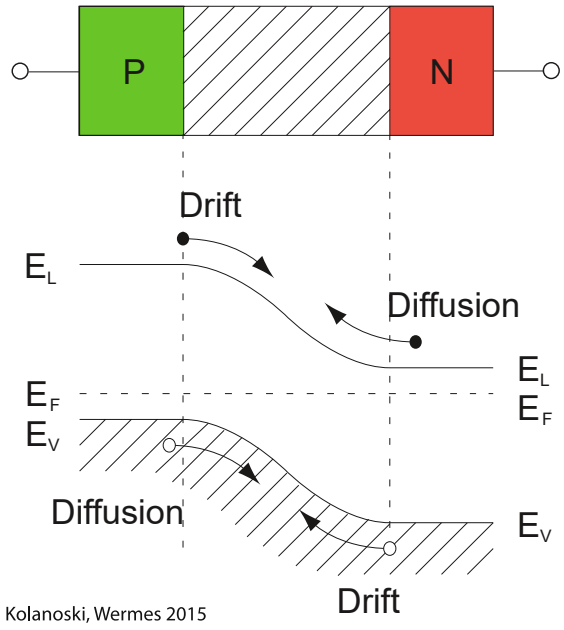

Figure 3.4.: Schematic of a PN-junction showing the energy levels in the depletion zone causing drift and diffusion.

When n- and p-doped semiconductors are brought into contact, the difference in densities between holes and electrons causes them to equalise, creating a region where both holes and electrons are depleted, also called the depletion zone. Due to the displaced charge, an electric field is created in the depletion zone. Applying a bias voltage to this PN-junction will either increase the size of the depletion zone further (reverse bias) or will decrease the depletion zone until a current can flow (forward direction). This basic functionality is called a diode. PN-junctions are the basis of a multitude of electrical components, from light-emitting diodes to solar panels, and play a central role in modern information technology. Depending on the momentum of the electrons in the bands, it can be differentiated between direct and indirect semiconductors. When used for particle detection, indirect semiconductors are chosen, meaning an external impulse from the incoming particle needs to be provided. Electron-hole pairs are then created inside the semiconductor through the effects described in Section 3.1. The electric field in the depletion zone will separate the charges and cause a current that can then be detected.

Signal Processing & Digitisation

The analogue signal created by a particle passing through the active area of a Silicon sensor is processed in order to digitally read out the detector. The signal is passed through a charge sensitive amplifier and then shaped using a band-pass filter. Digitisation of the

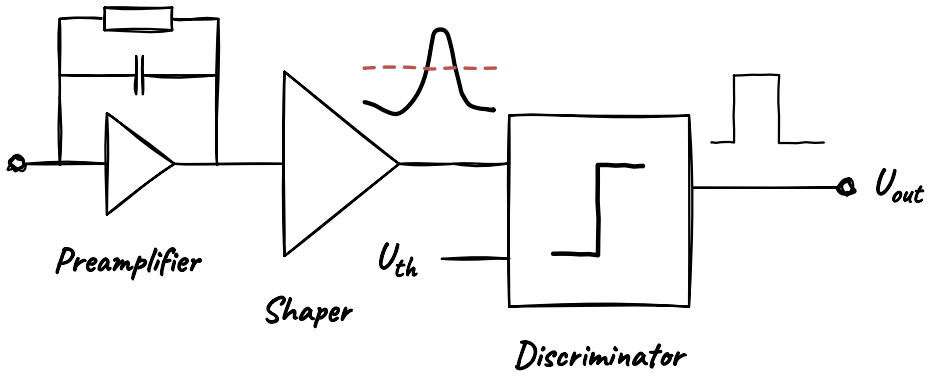

Figure 3.5.: Sketch of the FE functionality[5].

resulting voltage is done with the discriminator. Given a set threshold, it will output the time the signal is above this value. This is called Time over Threshold (ToT). Using a discriminator has the advantage of reducing noise while also preserving information about the deposited energy since the ToT is directly related to the collected charge. The different components of the readout system can be seen in Figure 3.5.

Spatial Resolution

Sensors of Silicon detectors can be segmented in different ways dependent on the desired resolution. Pixel detectors are divided into a grid of pixels roughly equal in length and width. This is opposed to Silicon strip detectors, where the width and length of a strip can differ by multiple orders of magnitude. No matter the layout of the segmentation, each pixel or strip requires a corresponding front end (FE) circuit for signal processing and digitisation. Different strategies can be chosen to make this circuit possible.

Hybrid Pixel detectors divide the detector modules into multiple subcomponents corresponding to their function. The sensor is made out of a Silicon wafer, which is segmented into many smaller pixels, with each pixel forming a PN-junction in which particles will cause an electrical signal. A bias voltage is applied between the top and bottom sides of the sensor. The read-out chip (FE chip) is an Application-Specific Integrated Circuit (ASIC) chip that contains all the needed circuitry to read out the signals from the pixels. This means all the analogue and digital circuitry for each individual pixel and peripheral logic for configuration and operation of the chip. The sensor and FE are connected on a per-pixel level using a process called bump bonding. The sensor and FE chip both possess metal connection pads for each pixel. A small ball of solder, called a bump bond, then

[5]Inspired by [17]

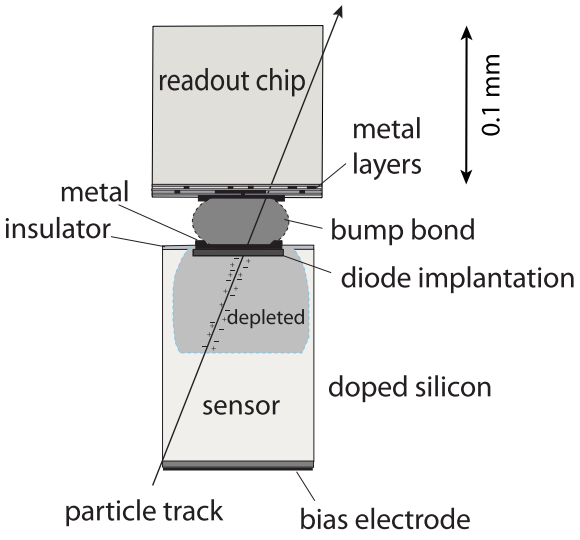

Figure 3.6.: Cross section of a single hybrid pixel cell[6].

connects all corresponding pads, forming a stack consisting of a sensor, bump bonds and FE chip. The layout of this stack for one pixel can be seen in Figure 3.6.

Monolithic active pixel sensors include both the active area of the sensor and the FE electronics on the same piece of Silicon. This innovative solution could reduce the required material budget and is an active topic of research.

Strip Detectors do not have the inherent challenge of pixel detectors, where a 2D grid of pixels needs to be read out in a very compact space. This means they can be read out by circuitry connected to the end of each strip [11].

[6]Image Source: Kolanoski, Wermes 2015 [17]

4. The ATLAS Inner Tracker

The ATLAS Inner Tracker (ITk) is part of the HL-LHC upgrade and will replace the current Inner Detector of ATLAS (see Section 2.1) with an all-Silicon design. It is designed to handle the higher luminosity of the HL-LHC, both in terms of increased data rates and radiation levels of up to $2 \times 10^{16}\,\mathrm{n_{eq}/cm^2}$. In addition, it provides improved resolution to maintain, or even enhance, tracking performance compared to the current ID, despite the more challenging operating conditions [24]. As shown in Figure 4.1, ITk is divided into different regions. Each region features different types of Silicon detector modules depending on their location and associated particle flux and pseudorapidity.

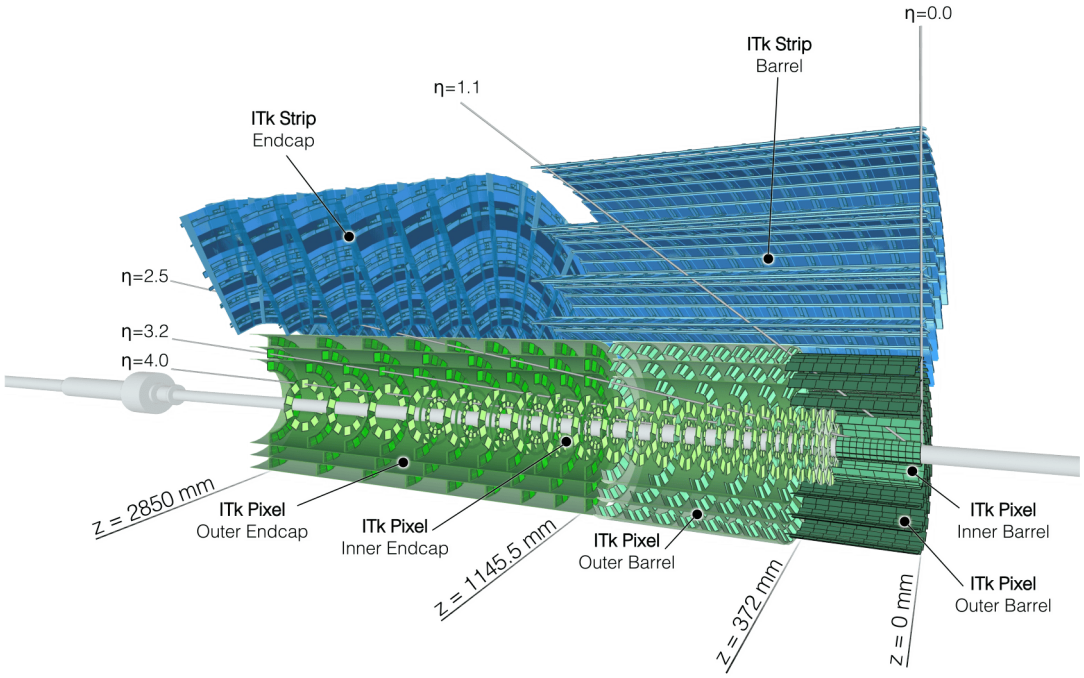

Figure 4.1.: Cutaway view of the ATLAS ITk detector with ITk Strips shown in blue and ITk Pixel shown in green. ©CERN

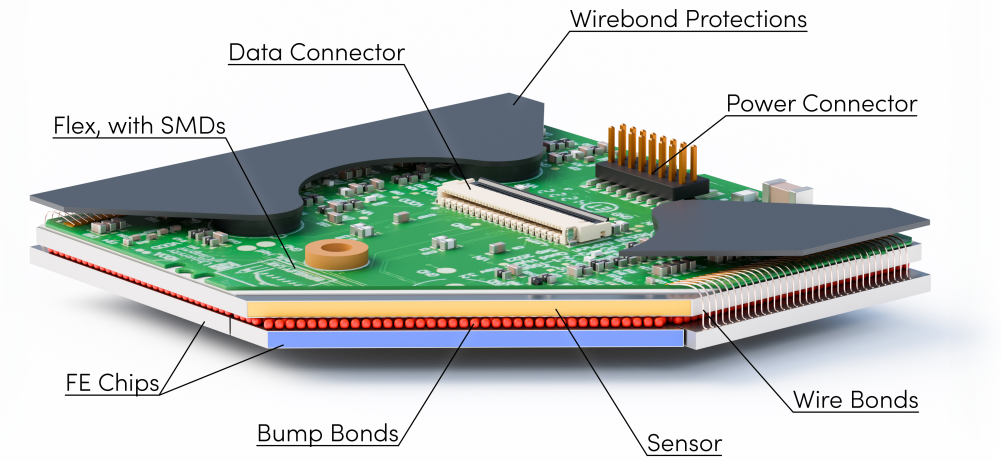

Figure 4.2.: Schematic of an ITk Pixel quad module showing different layers and components (bump-bonds and thicknesses not to scale)[1].

4.1. The ITk Strip Detector

The ITk Strip detector is made out of over 17,500 Silicon microstrip detector modules [25]. They follow a design as described in Section 3.4. The detector is divided into a barrel section made out of 4 layers and 6 layers of end caps, covering a region of $|\eta| \leq 2.5$.

4.2. The ITk Pixel Detector

The ITk Pixel Detector is located closest to the beam pipe. It is made up of more than 10,000 Silicon pixel detector modules arranged in 5 layers [3]. Within ITk Pixel, modules are again divided into different types depending on the region. The following chapters describe the features and functionality of quad modules and, more specifically, outer barrel quad modules. As the name suggests, they feature 4 FE chips bump-bonded to a single $4 \times 4\,\mathrm{cm}^2$ planar sensor [26]. The innermost layer of ITk Pixel is made of triplet modules, which consist of 3 FE chips with one $2 \times 2\,\mathrm{cm}^2$ sensor each. Due to their proximity to the beam pipe a 3D sensor is used [3]. Unlike the quad modules, the pitch of triplet modules varies, including $25 \times 100\,\mu\mathrm{m}^2$ and $50 \times 50\,\mu\mathrm{m}^2$.

4.3. ITk Pixel Quad Modules

The ITk quad modules are a hybrid pixel detector design as described in Section 3.4 [28]. They consist of 4 RD53 FE chips arranged in a 2×2 pattern and bump-bonded to one

[1] Image created by author using CAD model from [27].

sensor. Together they are called the bare Module. A flexible PCB (flex) is glued on top and wire bonded to the FE Chips. An illustration showing the different layers and components of a fully assembled outer barrel quad module can be seen in Figure 4.2.

4.3.1. FE Chips

While preproduction modules use the RD53B or ITkPixV1.1 FE chips, production modules use the RD53C or ITkPixV2 version [29]. Each FE chip consists of 400×384 pixels, leading to a total number of 153,600 pixels per module. These pixels are divided into so-called cores of 8×8 pixels, forming 48 core rows and 50 Core columns (CCs). Each core facilitates both the analogue and digital FEs of the pixels as described in Section 3.4. CCs can be turned on and off by adjusting four 6-bit integer values in the chip's configuration.

To set the threshold of the pixels, a digital-to-analogue converter (DAC) is used to output a reference voltage. An additional 4-bit trim value can be used to adjust the threshold of each individual pixel.

A further relevant feature of each pixel is the calibration injection circuit. This circuit enables the injection of signals into any pixel without the need to measure actual radiation. Two types of injections are possible: digital and analogue. This injection plays a crucial role during QC scans described in Section 4.5.

The periphery of the chip is located in the chip bottom close to the edge of the chip. The pad frame for wire bonding is located in the same region and placed closest to the chip's edge. There are 198 wire bonding pads in total.

The monitoring block is a part of the periphery that is especially relevant for module testing and tuning. It comprises an Analogue Current Multiplexer (IMUX) and an Analogue Voltage Multiplexer (VMUX), which feeds into an analogue to digital converter (ADC). This enables the digital readout of internal currents and voltages.

Serial Powering

Serial powering reduces the overall material budget and complexity greatly since modules can be wired in series, instead of receiving individual wires. The ITk detector will be the first of its kind to use this novel approach. While it offers the named benefits, serial powering can only supply a constant current to the module. Therefore a Shunt Low Drop-Out Voltage regulator (SLDO) needs to be used as part of the FE chips [30]. It is used to regulate the voltage and power supplied to each chip from the constant input current resulting from the serial powering chain.

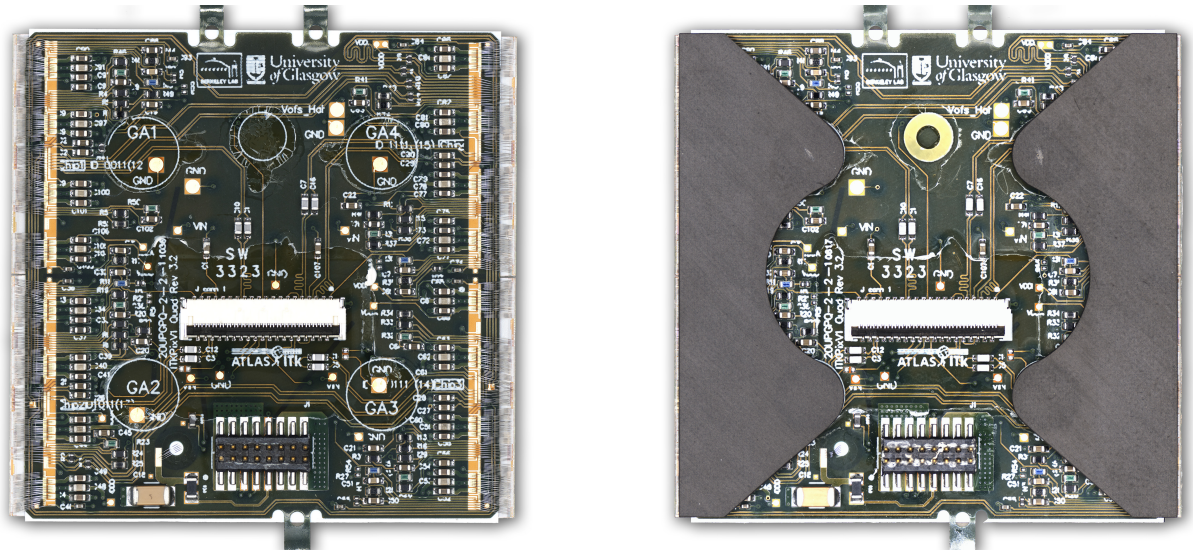

(a) (b)

Figure 4.3.: The top of a preproduction ITk pixel quad module without (a) and with (b) canopies.

4.3.2. Sensors

ITk Pixel quad module sensors consist of a $4 \times 4\,\mathrm{cm}^2$ large planar Silicon sensor with a thickness of 150 µm [3]. They are n^+-type implants in a p-type substrate, meaning a p-doped wafer with n^+-doped structures on it. The pixel pitch of the sensors is $50 \times 50\,\mu\mathrm{m}^2$, matching the pitch of the ITkPixV2 FE chips except for the central interchip region where the four chips bump-bonded to the sensor meet. In order to keep a distance between the chips, the pixel size is increased to $50 \times 100\,\mu\mathrm{m}^2$ or $100 \times 100\,\mu\mathrm{m}^2$ in this region.

4.3.3. Flex & Outer Barrel Wirebond Protection

To facilitate connectors and other passive SMD components, a flexible PCB (flex) is glued to the top of the bare module. Connection to the chips and sensor is achieved via wire bonds, which connect both data and power to the chips [28]. A detailed image of a typical topside of an ITk quad module can be seen in Figure 4.3a. There are two connectors. The power connector connects high voltage for biasing the sensor, low voltage for operating the FE chips, as well as allowing the readout of an NTC-type temperature sensor placed on the flex and enabling the low power mode of the module via one pin. The data connector allows transmission of the data coming from the FE chips [27]. During testing, these connectors are fitted with two ribbon cables called pigtails.

Additional regions of interest on the flex are the pickup points GA1 through GA4, which

all consist of a circular region 6 mm in diameter, free of any SMD components with a grounding pad located inside the region for pads GA1 and GA4 [27].
Outer barrel quad modules additionally receive so-called Outer Barrel Wire Bond Protections (OBWP or canopies) [31] which are needed to protect the module in further assembly steps detailed in Section 4.4. These Carbon fibre components are glued onto the 4 pickup points and partially cover the wire bonds as seen in Figure 4.3b. Additionally, a circular strain relief is attached to the flex to accommodate the pigtails expected later in the assembly.

4.4. Quad Module Production

Producing quad modules involves many different steps, drawing on both industry vendors and research sites around the world. Overall, over 10,000 quad modules will be produced, with 1,800 outer barrel quad modules being the responsibility of the ITk Germany cluster [32]. The German outer barrel cluster consists of the University of Bonn, the University of Göttingen and the University of Siegen, as well as the Max Planck Institute for Physics (MPP) in Munich, which provides facilities and equipment for parylene coating and is part of the inner system module production.
Bare modules are produced in industry by HPK, IZM[2] and Advafab, following standard semiconductor manufacturing processes in which the chips are initially located on a wafer and are then diced and thinned [33]. The sensor and FE chips are then bump-bonded in the hybridisation step, which involves applying solder bumps to one and placing the other on it in the so-called flip chip operation.
Once this step is completed, the bare modules are shipped to one of the assembly sites, which in the German cluster are Bonn and Siegen. The steps performed here are outlined

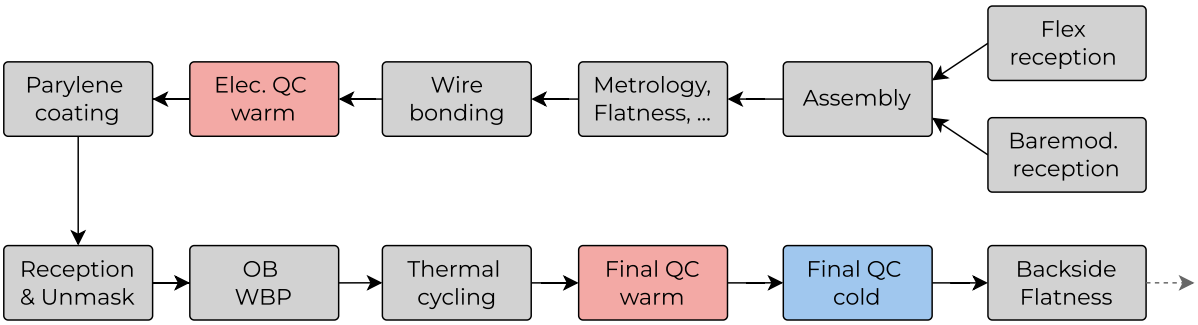

Figure 4.4.: Production and Testing scheme of Outer Barrel Modules.

[2]HPK: Hamamatsu Photonics K.K
IZM: Fraunhofer Institute for Reliability and Microintegration

in Figure 4.4. The flex is glued onto the bare module and wire bonded to the chips. From an electrical standpoint, the module is now complete and can be fully read out using the connectors on the flex.
Following an initial round of quality control tests, the module is then parylene coated. For modules from the ITk Germany cluster, this is done either commercially at APS in Paris, France or at MPP. Parylene coating is a vapour deposition process in which the module gets covered in a 5 µm thin polymer film protecting and insulating all electrical components [34]. During coating, all regions that need to stay free of parylene, such as the underside of the chips, and connectors for power and data, are masked using adhesive stickers, a Silicone mass or 3D printed caps.
After Parylene coating, the modules are returned and further processed at the sites in Bonn, Göttingen, and Siegen. They are demasked and the canopies are attached using two component Araldite glue [35] for mechanical attachment and a conductive silver glue to ground the slightly conductive Carbon fibre to the module via the pickup points. After this, the modules undergo extensive testing, which is described in Section 4.6 and concludes the production of a module.

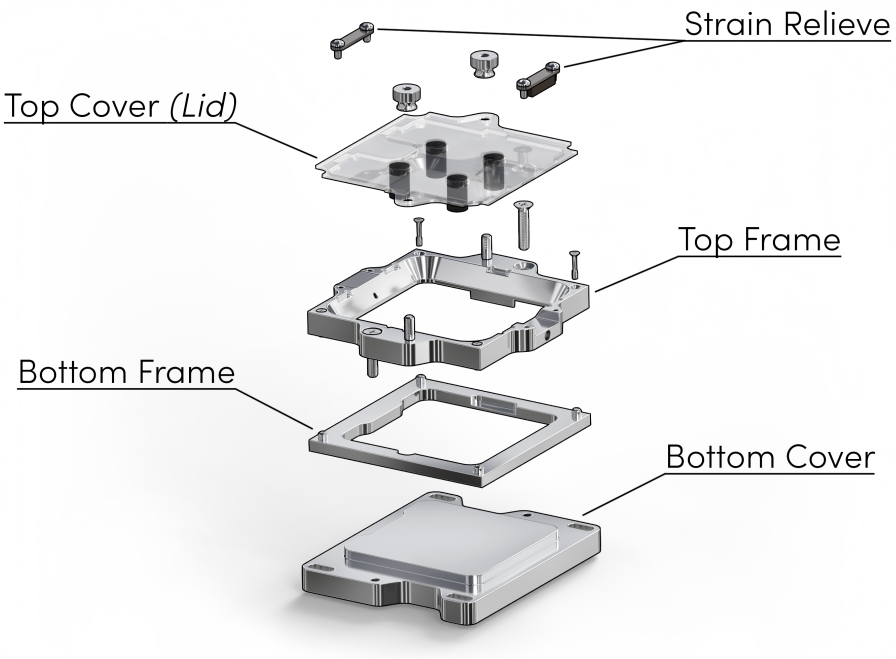

Figure 4.5.: ITk Pixel quad module carrier[3].

[3]Image created by author using CAD model from [36].

Carriers

After wire bonding, the modules are placed in a carrier, shown in Figure 4.5. This Aluminium component serves as a secure holder for modules during further testing and shipping. The carrier consists of four major parts [36]. The outside frame of the flex is placed securely between the top and bottom frames, therefore holding the module in place by clamping on the flex. The bottom cover provides a smooth surface for the FE chips to rest on and can be easily removed to perform tests. The top cover (lid) is made out of transparent plastic and protects the module from above. It additionally features four foam tabs, which apply gentle force to the pickup points of the module, pressing it onto the bottom cover. Finally, two strain reliefs are screwed onto the top frame, securing the data and power pigtails.

Cell Loading

Modules that are successfully assembled and pass all quality control tests are loaded into a local support structure, forming a loaded local support (LLS) [37]. During this process, modules are first glued to a piece of Carbon called a cell. This piece of Carbon serves as a thermal contact for later cooling the detector, which is a CO_2 cooling system keeping the modules at their operating temperature of $-15\,°C$. This assembly step requires the modules to be sufficiently flat, which is why flatness measurements described in Section 4.6.1 are necessary. During this process, the modules receive a new pigtail, that serves both power and data, which are folded as shown in Figure 4.6. The geometry of this assembly runs the risk of damaging the wire bonds, which is why wire bond protection is placed on the modules as described before.

Figure 4.6.: Physical model showing the positioning of Outer Barrel Modules on an LLS, including folded pigtail (orange) and OBWBP (black).

4.5. YARR

As a readout system for ITk Pixel Modules during the production phase, the "Yet Another Rapid Readout" (YARR) system is used. It supports both ITkPixV1 and V2 as well as a number of other readout chips [38].
YARR runs as software on the CPU of a given Data Acquisition (DAQ) machine. Readout of the modules is achieved via a Xilinx FPGA card that interfaces with the PC via a PCIe connection. Connection between the modules and the FPGA is achieved via DisplayPort cables.

YARR Scans

A central feature of YARR is the scan console [38]. YARR scans are an integral part of the module QC procedures detailed in Section 4.6.2. The functionality of the scan console is defined by JSON configuration files passed via command line argument. This includes the scan config, which defines what type of scan should be run and one or multiple connectivity files, which contain the information about the FE chips that should be scanned, including chip type, receiver (RX) and transmitter (TX) link numbers and the path to the configuration file of the chip. The following is a description of the scans used during normal QC operations [29, 32, 39]:

Digital Scans are used to test the digital part of the pixel FEs individually. This is achieved by commanding the discriminator to fire, emulating the output from a hit. For every injected signal one would expect one hit back (100 % hit occupancy). Since the digital part of the FE is not prone to noise, failed pixels can therefore indicate a communication issue with the module.

Analogue Scans also emulate hits across all pixels and expect the same number of hits back for each pixel. But instead of simply testing the digital part, a charge is injected into the analogue part of the FEs. Since this now also involves the preamplifier and signal shaping parts of the FE, the probability of failed pixels will be higher.

Threshold Scans measure a range of different charges injected into the analogue part of the pixel FEs. If the charge is underneath the threshold of the discriminator, no hit will be detected. If the charge lies above the threshold, a hit is detected. Ideally, if every pixel threshold was tuned perfectly to the correct charge and there was no noise, pixels below the threshold would never respond, and pixels above it would always respond. In

reality, due to noise the threshold will show a Gaussian distribution, where both the mean and the root-mean-square (RMS) determine the quality of the tuning of the pixels. For module QC, two different types of threshold scans are performed. High Range (HR) Threshold Scans have a larger range, with each step being measured less precisely. In High Definition (HD) Threshold Scans, the same step size is kept, but a smaller range is measured with an increased measurement precision.

ToT Scans measure the Time over Threshold at a given injected charge. During Module QC a charge of 6000 e is injected into the FEs. Similar to the threshold scan this scan will show a Gaussian distribution due to noise.

Noise Scans aim to detect overly noisy pixels that should be masked. Noise is a natural part of the analogue readout that occurs on all pixels, depending on the set threshold. However, some pixels might be overly noisy. To detect such pixels the chip is operated for a given time without application of radiation or charge injections. Pixels that show 10 hits after 10 million triggers will be considered noisy [39].

Threshold tuning calibrates the threshold of the discriminator to a set charge. This is achieved by injecting this charge into each FE and adjusting the threshold of the discriminator until the hit occupancy is 50 %. The tuning can be performed globally by adjusting the reference voltage provided by the DAC, or via the trim values of individual pixels. This is referred to as either global or pixel threshold tuning.

Disconnected & Merged Bump Scan use cross-talk to detect disconnected and merged bump bonds.
Cross-talk is caused by the proximity between pixels. When a charge is injected into one pixel, it will influence surrounding pixels and induce a signal in them as well. This allows us to inject charge into pixels indirectly simply by injecting in a pattern around the pixel. Unlike in analogue scans, where charge is directly injected into the pixel that is read out, in this way, a pixel will not respond if the sensor is not actually disconnected (disconnected bump). If two failing pixels are next to each other and still respond to $> 50\,\%$ of injections, it is a merged bump.

Self Trigger Source Scans measure actual radiation which the module is exposed to during this test. The required runtime of this test is dependent on the intensity of the source and can be set via the scans' configuration time. The test uses the self-triggering mechanism, which is also called the HitOR logic. This allows FEs to trigger

themselves when a particle is detected, making the scan much more efficient compared to sending triggers at a constant rate and hoping that the trigger randomly coincides with an incoming particle.

Core Column Scans are used to identify and solve CCs issues (further detailed in Chapter 7) effectively. This scan is similar to the analogue scan, but the CCs are turned on individually. CCs that show a high number of failing pixels are automatically disabled.

4.6. ITk Pixel Module Testing

Quality control testing (QC testing) is essential in ensuring ITk will meet its science goals by preventing faulty modules from being included in the detector. These tests include electrical tests, metrology and visual inspections. The following is a comprehensive list of all tests that are performed after Parylene coating and, therefore, relevant for the processes in Göttingen. Production has already started. However, the experience gained from initial module assembly and the rising pressure to stay on schedule mean that some of these tests might still be changed or removed from the QC procedure. This especially makes sense for tests that have a very high passing rate and/or tests that are made redundant by further processing steps.

4.6.1. Non-Electrical Testing

Visual Inspections

Visual Inspections involve taking images of the front and sometimes also the backside of the module. These images are then uploaded to the local database using a Python tool set which allows the user to step through smaller regions of the image, manually identifying possible issues [40]. Visual Inspections are done before and after demasking and after canopy gluing. Possible defects can include scratches on the FE chips, missing or squashed wire bonds, contamination, missing or damaged SMD components on the flex, scratches on the flex or damage to the copper traces on the flex and parylene on a pickup point or on other masked regions. After canopy gluing, the operator additionally visually checks the position of the canopies, making sure they stay within their envelope.

Metrology

Metrology involves the measurement of the module's dimensions and geometry. This involves two specific measurements:

After OBWP attachment, the total thickness of the module, including the canopies, is measured. Originally, this measurement also included a measurement of the thickness at the pickup points before OBWP attachment and measuring the thickness of the canopies themselves using a micrometre screw, which would allow for the calculation of glue thickness after attachment of the canopies. These two previous steps were dropped as of 2025 to simplify the process, relying on purely statistical data of the module and canopy thickness to determine the likely glue thickness from the total thickness [31].
In the final QC stage, modules undergo the backside flatness measurement, which measures the geometry of the 4 FE chips on the back of the module [39]. Backside flatness measurements are relevant for the attachment of the modules to the LLS described in Section 4.4.

4.6.2. Electrical Testing

Electrical tests are divided into simple electrical tests and pixel performance tests. As shown in fig. 4.4, both are executed in sequence at 20 °C for the Final Warm Tests and −15 °C for the Final Cold Tests as well as in the initial testing after wire bonding.

Simple Electrical Tests

Simple electrical tests both verify basic electrical functions of the module and calibrate internal electrical properties of the module. The simple electrical tests include the measurements and calibrations described in the following and are namely the IV-Scan, ADC Calibration, Analogue Readback, SLDO Qualification, VCAL Calibration, Low Power Mode Test and Data Transmission Test. A full account of all electrical tests and parameters can be found in [29, 39].

The IV-Scan is a crucial step in measuring the behaviour of the sensor. Bias voltages from 0 V to 200 V in 5 V steps are applied to the sensor and the corresponding current is measured. The observed characteristics should ideally be well behaved with no sharp increases or breakdown voltages.

The ADC Calibration is used to calibrate the Analogue to Digital Converter (ADC). The ADC of the module converts internal voltages into a 12-bit binary number. The ADC is used to measure all internal voltages and therefore it should be calibrated and its functionality be verified. This is done by measuring the ADC count against different input voltages.

The Analogue Readback test reads a number of internal voltages and currents from the ADC. For that, the voltage and current monitoring multiplexers are switched to different channels among the 64 available input channels. The ADC then measures the output of the multiplexers V_{mux} and I_{mux}. A number of different parameters, including supply voltages, trim values, reference voltages and more, are measured and compared to their acceptance criteria.

SLDO Qualification: As described in Section 4.3.1, the SLDO is a critical piece of circuitry enabling serial powering and regulating the current provided to the module. To verify the shunt is working correctly the input current is adjusted from 5.91 A to 7.56 A while measuring the chip's internal currents and voltages.

VCAL Calibration & Injection Capacitance: In order to perform scans, the injection of charge into the pixel FEs needs to be tested and calibrated. This includes the calibration of the injection voltage, which is controlled via the DAC and the measurement of the capacitance in the injection circuit. Together, the injected charge can then be calculated and controlled in the later scans.

The Low Power Mode operates the module at a reduced power with a voltage of $\approx 1.5\,\text{V}$. This allows the module to be operated in a limited manner without cooling once installed inside the detector. The chips are configured using the LP configuration files and internal voltages and currents are measured. A digital scan is performed to check the connectivity to the module.

The Data Transmission test determines the usable width of the binary symbol of the digital output of the FE chips. This is called eye width. It is the valid sampling window in the serial communication. A sufficient eye width is critical to ensure stable communication with the chips.

Pixel Performance Tests

Pixel performance tests consist of a defined set of YARR scans. They are grouped into 3 test steps: Minimum Health Tests, Tunings and Pixel Failure Analysis [39]. The separate scans are described in detail in Section 4.5.

Minimum Health Tests (MHT) are meant as a fast test of the functionality of the FEs. It consists of:

- A digital scan
- An analogue scan
- A threshold scan (hr)
- A ToT scan

Additionally, one might perform a CC scan to ensure defects are caught before testing begins.

The tuning step (TUN) validates that the discriminators' reference voltage can be tuned. Tuning of the detector will be done regularly when it is in operation. Therefore, the ability to tune modules needs to be tested. The tuning scans include:

- A threshold (hr) & ToT scan measuring the performance before the tuning
- A global threshold tuning
- A global preamp tuning
- A pixel threshold tuning
- A threshold scan (hd) & ToT scan after tuning

The tuning performance is considered passed if the tuned mean threshold is within 100 e of the target with an RMS of < 50 e.

The Pixel Failure Analysis (PFA) is performed to evaluate the final performance of the module. The tests include:

- A digital scan
- An analogue scan
- A threshold HD scan
- A noise scan
- A disconnected bump scan

- A merged bump scan
- (A self-trigger source scan)

Together they create a mask of pixels that are disabled due to the specified QC criteria not being met. One speciality of the PFA that is only performed in the final cold stage is the self-trigger source scan, where the module is actually exposed to a radiation source, and its response is measured.

Thermal Cycling

During the lifetime of the detector, the CO_2 cooling systems of ITk will be turned on and off multiple times, leading to large temperature variations. To ensure no significant damage is caused by these variations, the modules are thermally cycled before the final QC steps. This test verifies that the module can, in principle, survive this temperature fluctuation [29]. Additionally, a cold power-up test is performed to ensure modules can be powered on from a starting temperature of $-45\,°C$.

Local & Production Databases

In order to keep a record of the work done at different testing sites, the data resulting from QC testing, as well as the components involved in the assembly process and configuration files of the modules, are tracked using a central Production Database (PDB) [41]. Before test results are uploaded to the PDB, they are uploaded and analysed in the Local Database (LocalDB)[4]. The LocalDB acts as a buffer stage between the actual testing performed locally and the PDB. Operators at each site can view and check the tests performed at their site. Results from all tests are analysed directly by the local DB and checked against the pass-fail criteria. Once a testing stage is complete, the operator can sign off which tests should be used to evaluate the performance of a module in a given stage. The data is then pushed to the PDB.

[4]More information on: https://atlas-itk-pixel-localdb.docs.cern.ch/

5. Production Infrastructure & Processes in Göttingen

To perform the production and QC steps described in Section 4.4, numerous setups and procedures are employed. The following is a description of the infrastructure in Göttingen, as well as the measures taken to ensure an efficient high-throughput production. Estimates of the maximum weekly production rate are made, where applicable. Since the throughput is highly dependent on personnel availability, it is distinguished between a *sustainable rate* and a *peak rate*. The sustainable rate assumes personnel availability of roughly eight hours for five days a week, while the peak rate assumes around 12 hours a day, six days a week.

5.1. OBWBP Gluing

The attachment of OBWBP (canopies) is performed using a centrally provided gluing fixture [42] shown in Figure 5.1. The fixtures consist of an upper and a lower part. The module is placed on the lower part and the canopies on the upper part. Glue is applied to the canopies' pillars, and the two fixtures are placed on top of each other. During this procedure, both the module and canopies are held in place via vacuum pressure.

Modules are completely removed from the carrier for the gluing. Therefore, additional care needs to be taken to not damage them. Issues with the removal from the carrier were encountered, in which parylene prevented the separation of the top and bottom frames (see Figure 4.5) of the carrier. A 3D-printed tool, developed as part of this thesis, solves this issue by applying force between the components in a safe manner.

Two additional gluing fixtures have been taken into operation. For this, new tubing and valves were configured and a custom-designed 3D-printed valve block was created. The newly received tooling has been validated using Silicon dummy modules, qualifying them for production.

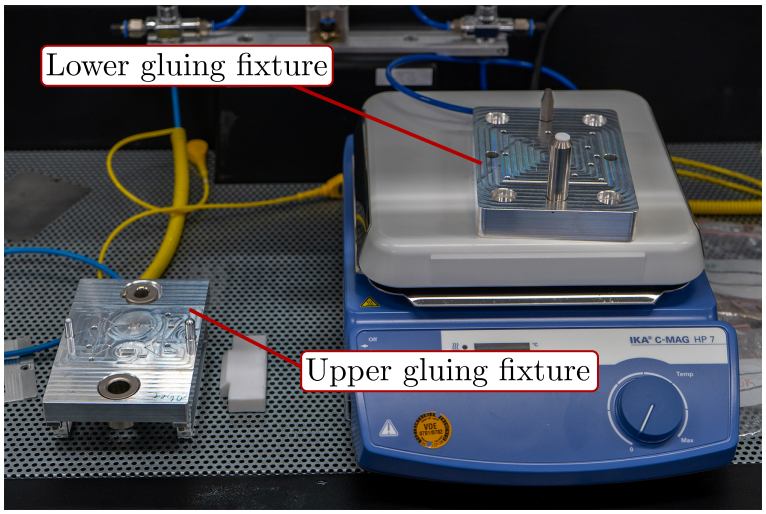

Figure 5.1.: Fixtures used for OBWBP gluing. The upper gluing fixture received the canopies. The lower gluing fixture holds the module. Holes for alignment pins are present in both. The upper fixture fits on top of the lower fixture.

OBWBP Gluing Throughput

The throughput of the OBWBP gluing is mainly decided by two variables: The curing time of the glue and the number of fixtures available. As part of the work done during this thesis, a solution to increase the module throughput has been proposed: Heating the assembly to a temperature of 40 °C during the curing process reduces the cure time from 8 h to 3 h [35]. The maximum throughput can be seen in Table 5.1. While the current number of installed chucks is three, it is expected that further chucks will be delivered in Q1 2026, bringing the total to four chucks.

Table 5.1.: Estimation of the maximum production throughput of OBWBP gluing.

	Sustainable Rate		Peak Rate	
	No Heat	Heated	No Heat	Heated
3 Chucks	15 mod/week	30 mod/week	30 mod/week	45 mod/week
4 Chucks	20 mod/week	40 mod/week	40 mod/week	60 mod/week

5.2. Visual Inspections & Metrology

Visual inspections and metrology of the modules are done at multiple stages across the production process in Göttingen. Visual inspections aim to ensure any physical damage is documented. Metrology ensures that the module geometry lies within the specified parameters and guarantees that cell loading and cell integration can be performed successfully.

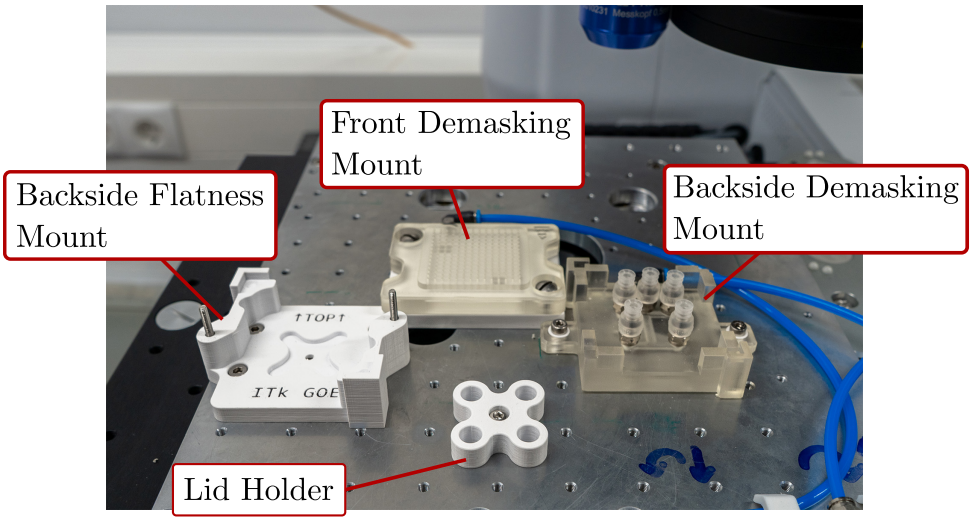

Figure 5.2.: Layout of the work surface of the *Micro-Vu Vertex 261* metrology machine, optimised for ITk pixel module production. All fixtures are positioned such that they can be reached by the relevant toolheads.

All these steps are performed on a *Micro-Vu Vertex 261* metrology machine. It is equipped with three tool heads: a camera with a resolution of 0.5 µm, a laser scan head and a touch probe, which have a precision of up to 2 µm.
The mountings required for production are fitted on the work surface permanently (see Figure 5.2). This reduces the downtime of the machine by eliminating the need for repeated setup and calibration steps. This is made possible by arranging the mounts, using custom-designed 3D-printed spacers and adapters.

Visual Inspections & Metrology Throughput

Each measurement takes between 10 min and 15 min. In total three inspections need to be performed per module. The data taking is semi-automated but requires a human to be present at all times. This means the throughput is directly dependent on the time spent operating the machine. Assuming the machine can be staffed for 40 hours/week, the expected throughput is ~ 60 modules/week.

Reception & Visual Inspection

After receiving the modules from the parylene coating, they need to be demasked and visually inspected. Images are captured before and after removing the masking stickers on both the front and back sides of the modules. The mounts required for demasking are placed on the metrology machine. This enables repeatable and easy capturing of

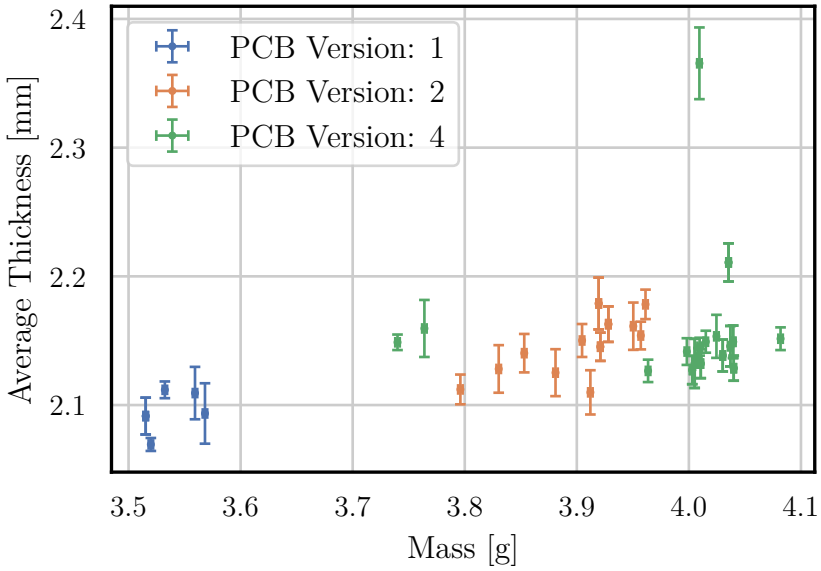

Figure 5.3.: Total module thickness vs. module mass after canopy attachment. Both the measurement uncertainty of the weight at 0.1 mg and of the height at 2 µm are negligible in this figure. The displayed error is the standard deviation of the thickness at the four pickup points.

the required images, making the process more reliable and enabling the use of the same demasking fittings for other measurements.

Post Canopy Inspection

Inspections after the OBWBP attachment are performed reusing the front demasking mount, making efficient use of the available tooling. A visual inspection is performed and the total thickness at the 4 pickup points is measured using the laser scan head.
Figure 5.3 shows the average thickness across the 4 pickup points against the total mass of the module. The data consists of 48 modules, including preproduction and production modules, that are present in the LocalDB. One can see that flex PCB version 1 forms a separate cluster from the other versions, since it is thinner. One outlier with a larger thickness can be seen as part of flex version 4.

Backside Flatness

Backside flatness measurements were originally performed on a mount designed to use a vacuum to hold the module during the measurements. Concerns about deformation from the vacuum pressure meant this device could no longer be used.
A 3D-printed holder was developed and is shown in Figure 5.5. The holder has an in-

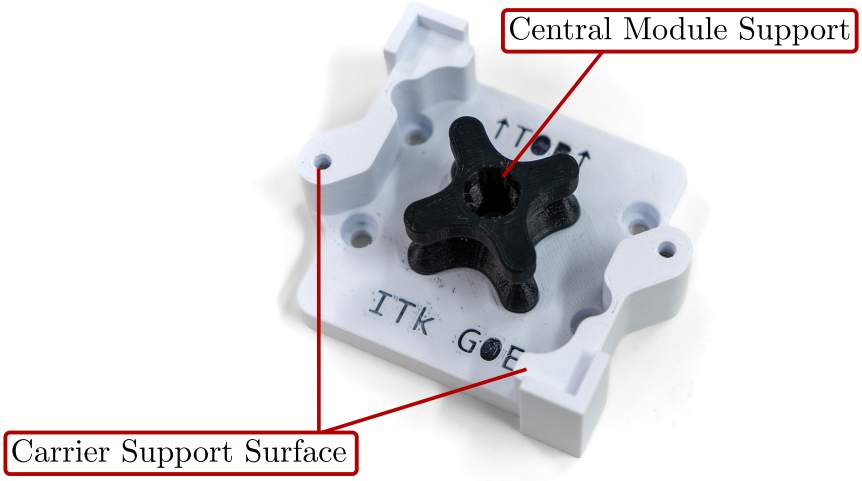

Figure 5.4.: 3D-printed fixture for backside flatness measurements. The central module support is an interchangeable component that can be removed or adjusted as needed. The module carrier rests upside down on the outside frame.

terchangeable support column in the centre. The central support is made from a flexible plastic (TPU), allowing it to hold the module level and apply as little force as possible. Different support columns are tested, varying the height, geometry, and material stiffness, iteratively in an attempt to reduce the force applied to the module and therefore minimize bowing.

Improvements in the programming of the machine enable measurements entirely without the central support, by measuring the flatness even when the module is not laying perfectly level. This solution causes minimal deformation of the module. The holder offers various other benefits, including reduced operational complexity and less risk of damaging the module during the measurement.

Results of Backside Flatness Measurements

For each backside flatness measurement, a flat plane is fitted to the measured point cloud, and the out-of-plane deviation d_z is calculated. The relevant QC parameter is the range of values of the plane deviation $\Delta d_z = \max(d_z) - \min(d_z)$ across the module. Values below 50 µm are categorized as green and pass the QC test, values above 50 µm and below 100 µm are yellow and anything above 100 µm is red, which means the test fails [43]. Results of backside flatness measurements performed during production can be seen in Figure 5.5. Each measurement can be seen as a high-dimensional vector. Applying principal component analysis (PCA) yields a one-dimensional embedding. This is displayed on the x-axis to create a visual separation between the modules that groups

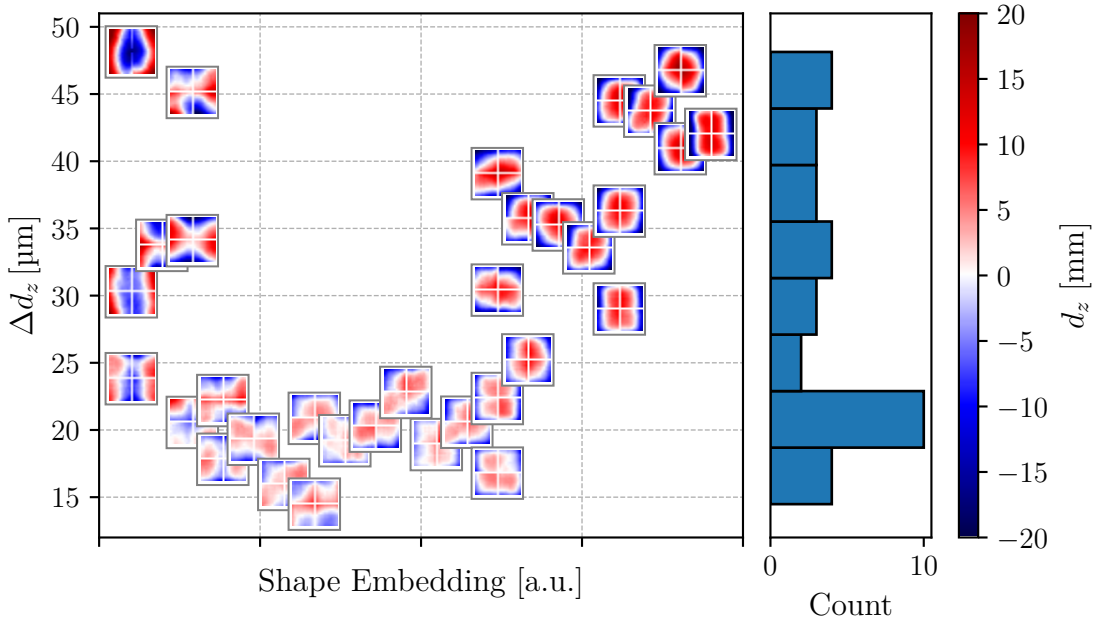

Figure 5.5.: Results from backside flatness measurement showing the range of the out-of-plane deviation Δd_z and the shapes of the modules' backside in the form of inset images. PCA embedding is used to group similarly shaped modules.

similar modules together, while the y-axis displays Δd_z. It can be seen that all modules fall well below 50 µm, with a peak at 20 µm. Additionally, one can notice that a majority of modules have a convex backside shape. This is a feature resulting from the production process. For modules with smaller out-of-plane deviations, shapes become more irregular, with the individual chip geometry having a stronger influence. Some modules with a concave shape are located towards the left of the plot, but represent a minority of modules.

5.3. Thermal Cycling & Cold Power up

Thermal cycling is performed using a *Vötsch VT 7012 S2* thermal shock chamber. It contains two chambers that can be independently heated or cooled and set to different temperatures. A basket is moved between the chambers to induce a thermal shock. As this mode of operation leads to drastic temperature changes, during regular operation, only one chamber is used to adjust the temperature more slowly. The setup contains four vacuum holders for thermal cycling and four additional slots for cold power-up tests. The chamber is not only used for module production but also for thermal cycling studies, as shown in Chapter 7, and for testing cables as part of ITk.

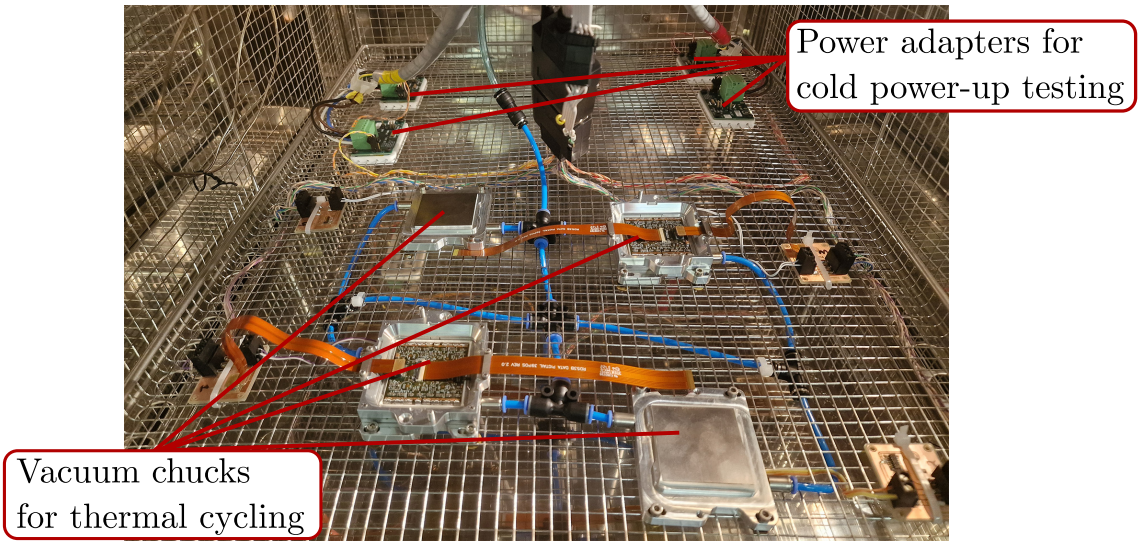

Figure 5.6.: Interior of *Vötsch VT 7012 S2* thermal shock chamber used for thermal cycling and cold-power up testing during production, as well as for the CC study described in Chapter 7.

Throughput of Thermal Cycling

Thermal cycling takes approximately four hours. This leads to a sustainable rate of 40 modules/week and peak rate of over 70 modules/week. This number might be diminished while the setup is used for other purposes. Potential upgrades to the system could increase the throughput by a factor of two.

5.4. Electrical Testing

Electrical testing is performed in two setups. The *Climate Chamber* (further detailed in [44]) and the *Source Box* (further detailed in Chapter 6). Both setups contain four test slots. Since the climate chamber has no active temperature regulation, it can only perform warm tests of modules. To perform the Final Cold testing, including a source scan, the Source Box is needed. Testing is fully automated and utilises a queue system, meaning tests can run fully independently during nights and weekends. Modules that fail tests might need to be debugged in a more manual process.

While only Final Warm and Final Cold testing is required during production, additional testing might be performed after post-parylene reception and after OBWBP gluing to gain a deeper understanding of the production yield and failure modes observed.

Table 5.2.: Throughput of Final Electrical QC with different numbers of FPGAs employed at the Source Box and optionally running Final Warm tests in the Climate Chamber.

FPGAs at Source Box	Final Warm in Climate Chamber	Sustainable Rate	Peak Rate
1	No	30 mod / week	36 mod / week
	Yes	40 mod / week	60 mod / week
2	No	40 mod / week	55 mod / week
	Yes	60 mod / week	78 mod / week
3	No	50 mod / week	60 mod / week

Throughput of Electrical Testing

While both setups are capable of parallel operation, as shown in [44], executing electrical tests in parallel does not yield significant improvements in the required test times.
The throughput is therefore highly dependent on the number of available readout FPGA systems, as well as the distribution of tests between the two setups. Table 5.2 shows the throughput for different models. It is assumed one set of electrical QC tests takes 90 min each for warm and cold testing and an additional 30 min for the source scans. It can be seen that rates well above 30 modules/week, with potential peak rates of 60 modules a week or more, can be achieved. It is important to note that this assumes no debugging of modules, meaning that if a module fails tests it is disregarded and not further processed. Manual debuging of modules and additional testing will decrease the the throughput.

6. Test Stand for Electrical Testing with Source Scans

To facilitate the electrical testing of ITK Pixel modules during production, a new test stand has been constructed as part of this thesis. The main goal of the setup, which is referred to as *The Source Box* or *The Box*, is to maximise the module throughput of the electrical testing steps. This is achieved by enabling automated testing of up to 4 modules that can be installed on independent testing mounts at the same time. Additionally, the design and operational complexity are kept to a minimum, leading to high reliability and minimal downtime. For the electrical QC testing, several subsystems are required[45]:

- **Temperature Regulation:** The modules are tested at two distinct temperatures. Warm at 20 °C and cold at −15 °C. Means have to be implemented to keep the modules at the specified temperatures as well as dissipate any heat generated by the modules.

- **Environmental Monitoring:** To ensure modules are in a safe operating condition their temperatures and test chuck conditions need to be monitored. Interlocks need to be present to prevent any damage to the modules or the setup itself, caused by environmental factors like overheating or condensation.

- **Radiation:** As one of the tests in the electrical QC is a source scan, a radioactive source needs to be automatically positioned above the module during certain periods of the testing. To protect personnel, this means the box needs to create a radiation seal around the test area and prevent any personnel from being exposed to radiation.

- **Power & Data:** The modules need to be provided with both high and low voltage power, both routed through a power adapter card. Data from the module needs to be routed to a readout FPGA using an adapter card.

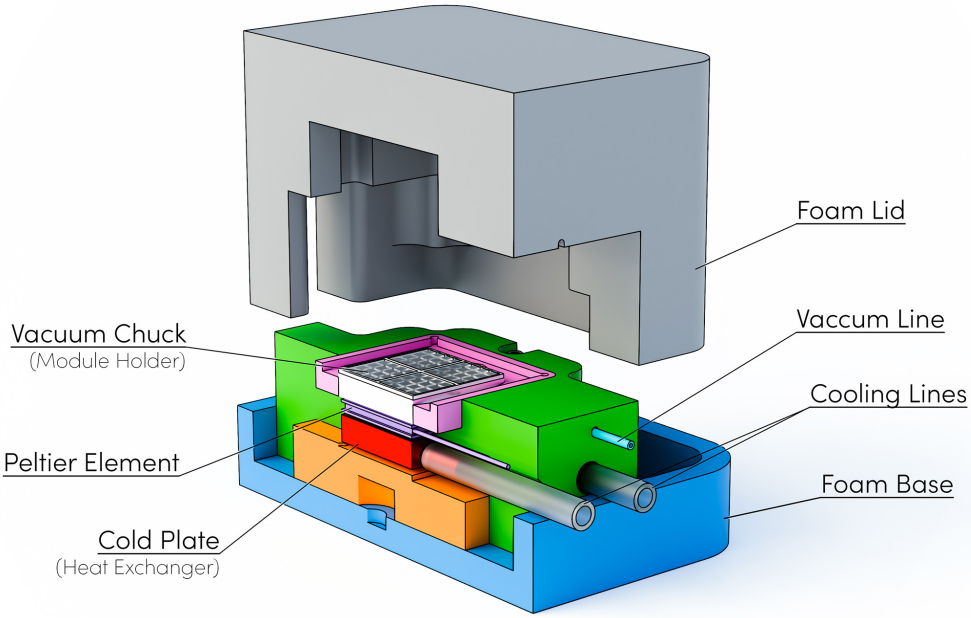

Figure 6.1.: Cross-sectional view of an ITk cooling chuck unit. In the centre, the cold plate, the Peltier element and the vacuum chuck are visible.

6.1. Module Cooling Unit

The source box setup uses the quad vacuum chuck cooling unit to mount and cool the modules during electrical testing. It is designed to facilitate electrical testing with active temperature regulation and is made available centrally to ITK pixel module production sites. A cross-sectional view of the design can be found in Figure 6.1.

The module is placed on the vacuum chuck, which is located above a Peltier element. The Peltier element is used to actively regulate the temperature of the module, while the applied vacuum ensures good contact between the module and the chuck. The heat is dissipated from the bottom of the Peltier element with a heat exchanger, called cold plate, that is connected to a temperature control unit via tubing filled with silicone oil. A lid is placed above the module during testing to allow dry air to be flushed into the system. This prevents any condensation from forming at low temperatures.

To monitor the condition of the chuck, various sensors are used: *PT1000* temperature sensors are applied to the cold plate and vacuum chuck. An *SHT85* sensor measures the ambient air temperature, humidity and resulting dew point. The module temperature is monitored via its onboard NTC. The vacuum pressure is measured using an *SMC ZSE30A*.

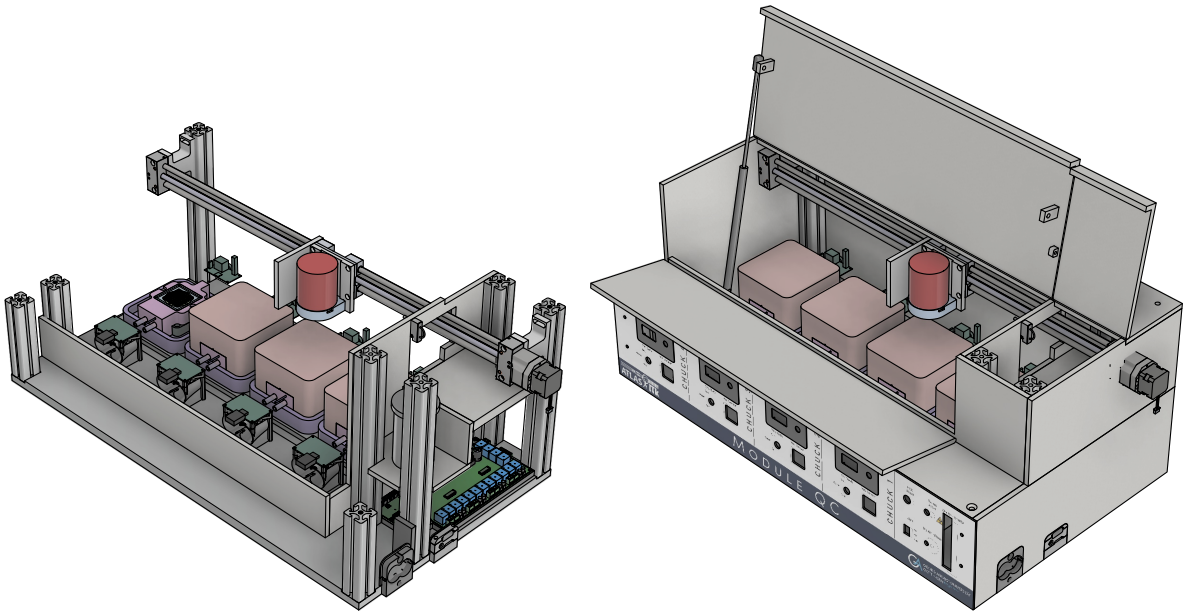

Figure 6.2.: 3D representations of the Source Box, showing the internal structure (left) and the fully assembled teststand including the external walls (right).

6.2. Overall Layout & Construction

The overall layout of the test stand is designed for the production of ITk pixel modules using the previously described test chucks and is not primarily designed as a general purpose setup.

It can be seen in Figure 6.2. The construction of the box uses an Aluminium T-slot extrusion skeleton mounted to a baseplate. This forms a robust internal structure for mounting the walls and components to. The material choice of the base and the sidewalls is detailed in section 6.3.

A design is chosen that is optimised for minimal complexity, ease of use and both passive and active radiation safety. The box can be divided into multiple areas: The main volume is where the four test chucks are located. It can be closed by hinged top and front access panels, which lift up and drop down, respectively. As shown in Figure 6.3, the front access panel only covers the top half of the front face, with a control panel below. Behind the control surface, a routing area for electronics and tubing is located. It features a labyrinth into the main volume of the box, which allows routing of services while ensuring a radiation seal. The geometry of this assembly ensures that even with the lids open, the downward-facing radiation stays in the envelope of the box and personnel standing in front of the box are not exposed. This adds a passive layer of safety to the box, in

[1]Detailed technical drawings in Appendix A & Full CAD Project under https://a360.co/4fRXbN9

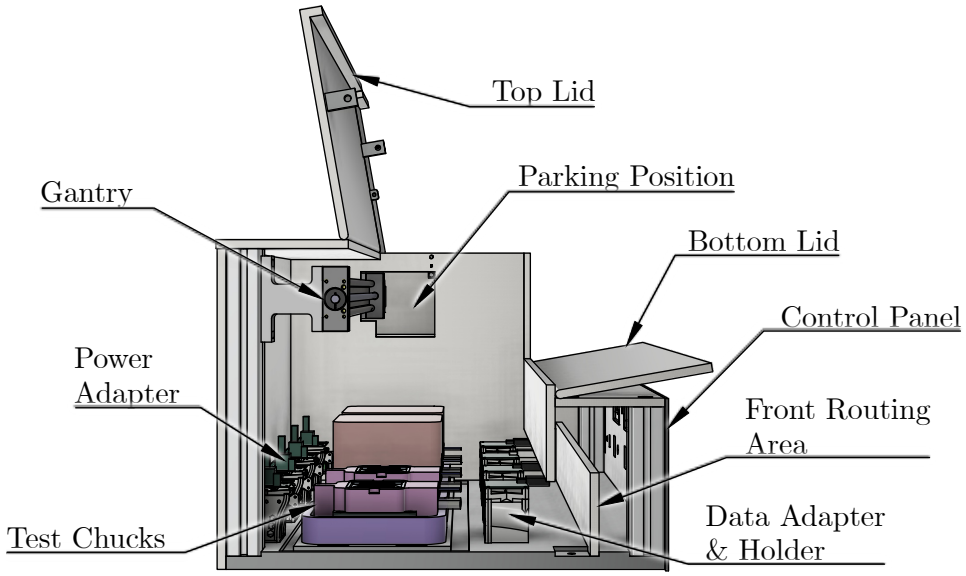

Figure 6.3.: Cutaway view of the left side of the box, showing the internal division into main volume and front routing area[1].

case the active safety mechanisms described in Section 6.3 were to fail. Additionally, this design leaves ample room to access the test chucks from above and unifies all controls on the front, meeting the goals in terms of usability.
To the right, a separated containment area for the radioactive source is located. It can be accessed only by authorised personnel using a padlock and allows for the installation and removal of the radioactive source. Since this area is completely isolated from the main volume, the source does not need to be removed during handling of the modules, reducing both operational complexity and increasing safety. Underneath the containment area, an additional space for electronics is located.

6.3. Radiation Safety Considerations

To ensure personnel safety, the outside material of the box needs to absorb the radiation of the 8 MBq ^{90}Sr-source to a dose below 0.5 µSv/h[2]. When the β-radiation hits any absorption material, the electrons interact as described in Section 3.1. While the β-radiation gets absorbed, secondary radiation in the form of bremsstrahlung photons is created as a function of $\sim Z^2$. This secondary radiation also needs to be absorbed.
Multiple materials are considered for the test stand. These include solid materials like Aluminium and Steel, as well as an Aluminium + Lead + Aluminium sandwich that aims to place Aluminium, a low-Z-material, facing the radioactive source, reducing the

[2]In accordance with §52 StrlSchV (Germany).

Table 6.1.: Possible construction materials of the test stand and the required material strength, including safety margins and rounded up to a standard gauge.

Material	**Thickness** [mm]
Aluminium	30
Steel	10
Alu + Lead + Alu	2 + 2 + 2

amount of bremsstrahlung created, followed by Lead, a high-Z-material, that absorbs any remaining radiation. To evaluate the performance of the materials, two independent theoretical evaluations and real absorption tests are performed. The material thickness determined to be suitable for use as an absorption material can be found in table 6.1.

Each option is considered regarding weight, cost, machinability and availability. For the side walls 1 cm thick steel is selected, due to its cost effectiveness as well as its availability and its use in the previous test stand, making it a proven design. For the ground plate, a 2 cm Aluminium Base on top of a 3 mm Lead plating is chosen. Since Aluminium is easily machinable, it has excellent properties to mount all other components onto. Placing it on a Lead plate effectively creates an Aluminium + Lead sandwich without having to invest in specialised materials.

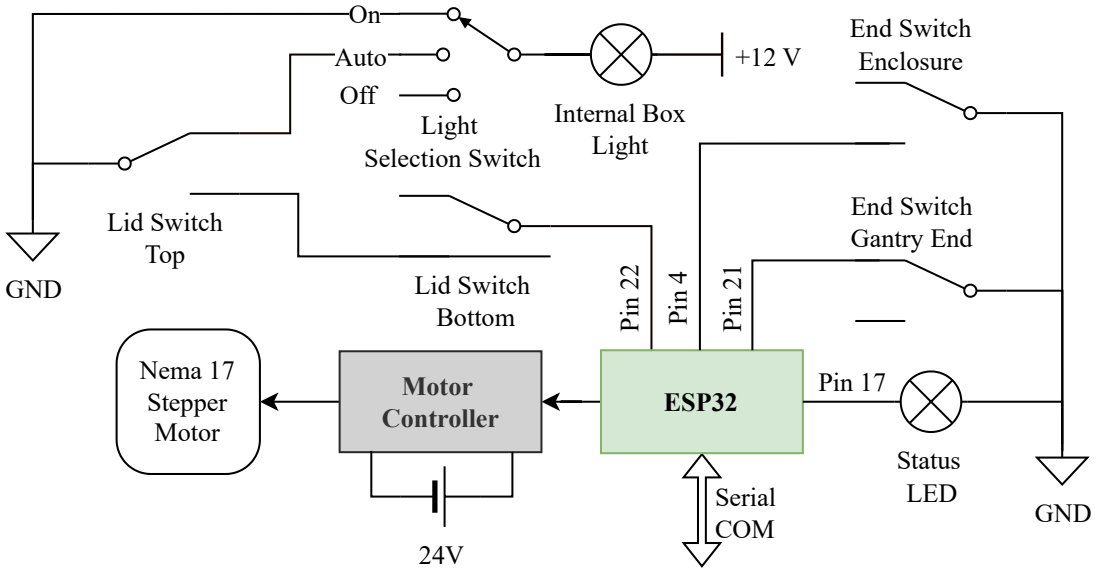

Figure 6.4.: Wiring diagram of the gantry control electronics. An ESP32 (green) is connected to endswitches and a motor controller via GPIO pins. It communicates with a computer via Serial COM.

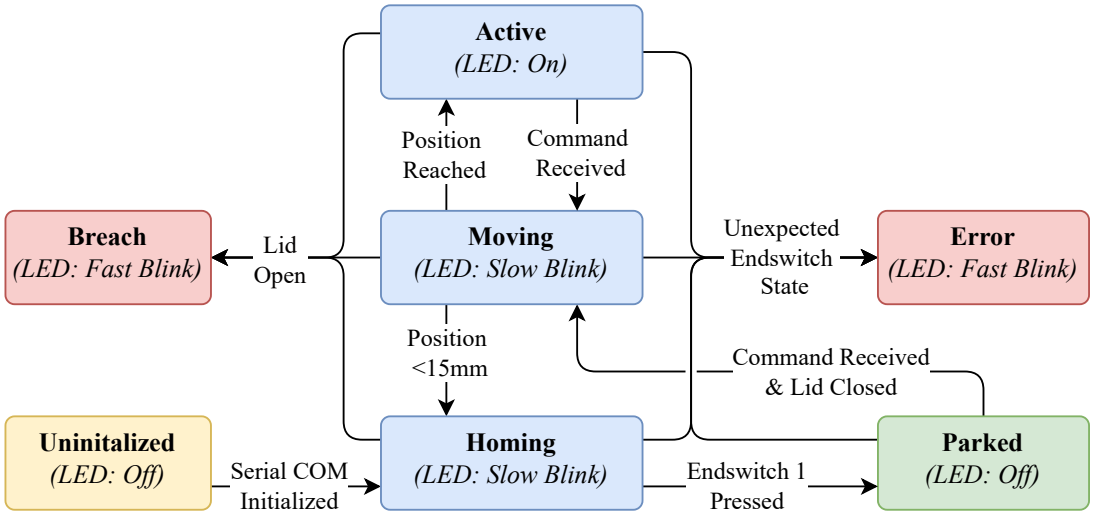

Figure 6.5.: State machine logic of the source control firmware. States in Red indicate an error, states in blue indicate the source is within the main volume.

Gantry System

The gantry system's function is the positioning of the radioactive source above the modules, in a safe and reliable way. By placing all test chucks along one line a one axis gantry system is usable instead of a two axis gantry, simplifying the design. A spindle-driven system, that is powered by a stepper motor, is selected. As described in Section 6.2, the source can be moved into a shielded containment area. This solution is chosen, since it adds no movable parts onto the gantry arm and therefore offers minimal complexity. It is also the safest solution, because the space underneath the source is never accessed during operation.

Gantry Motor Electronics & Control Logic

The gantry system is controlled via an *ESP32* microcontroller. It sends signals to the stepper motor controller and tracks the state of the source box via multiple contact switches, as shown in Figure 6.4. One contact switch in the containment area is used to calibrate the position of the gantry and ensure the gantry is in the containment area. Another set of switches determines whether the box is open or closed. The firmware of the ESP32 runs a state machine logic, which is displayed in Figure 6.5. It keeps track of the current position of the source and ensures that the source never leaves the containment area while the box is opened and reports any anomalous behaviour. The ESP32 is connected to a Python interface, via serial communication, running on a computer. It receives commands from the PC and reports back the current state.

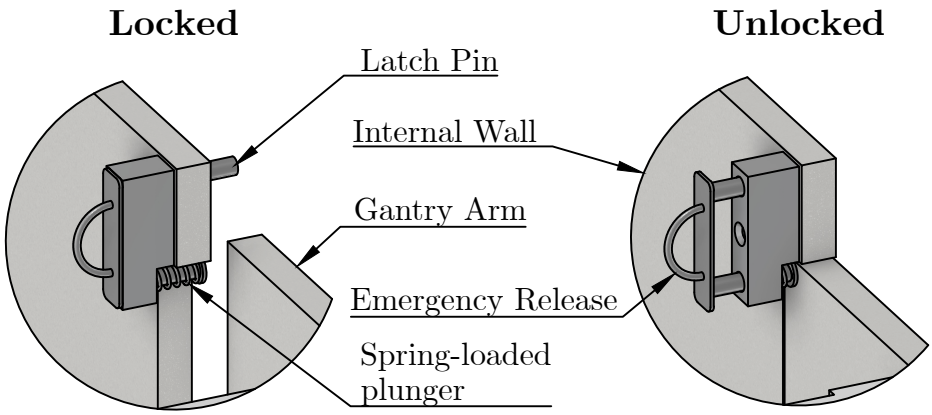

Figure 6.6.: Visualisation of the mechanical radiation lock in the locked and unlocked state. This assembly is located at the internal wall shielding the containment area. It is viewed from the back for better visibility.

Mechanical Radiation Interlock

While the radioactive source is positioned in the main volume of the box, it needs to seal itself shut, to prevent personnel from accidentally opening the box and being exposed to radiation. Different choices of different locks were considered.

Multiple types of electronic solutions can be purchased off the shelf. For all electronic solutions, it is critical that in the event of a power failure, the box remains locked. Additionally, all electronic solutions rely on either the state of a contact switch and/or the internal state machine logic of the motor control script, which both lead to additional failure points and complexity.

To avoid these issues, reduce the complexity and keep the number of possible failure points to a minimum, an alternative solution is implemented. This custom assembly is shown in Figure 6.6 and is located at the interface wall between the containment area of the source and the main volume of the box. It consists of a spring-loaded pin that the gantry arm itself pushes back while moving into the containment area to unlock the box. This novel solution avoids electronics altogether, making it power independent in both the open and closed positions. The assembly is also simple to manufacture in-house, making it very cost-effective. Additionally, it allows emergency access to the main volume of the box by first accessing the containment area and pulling the pin back manually.

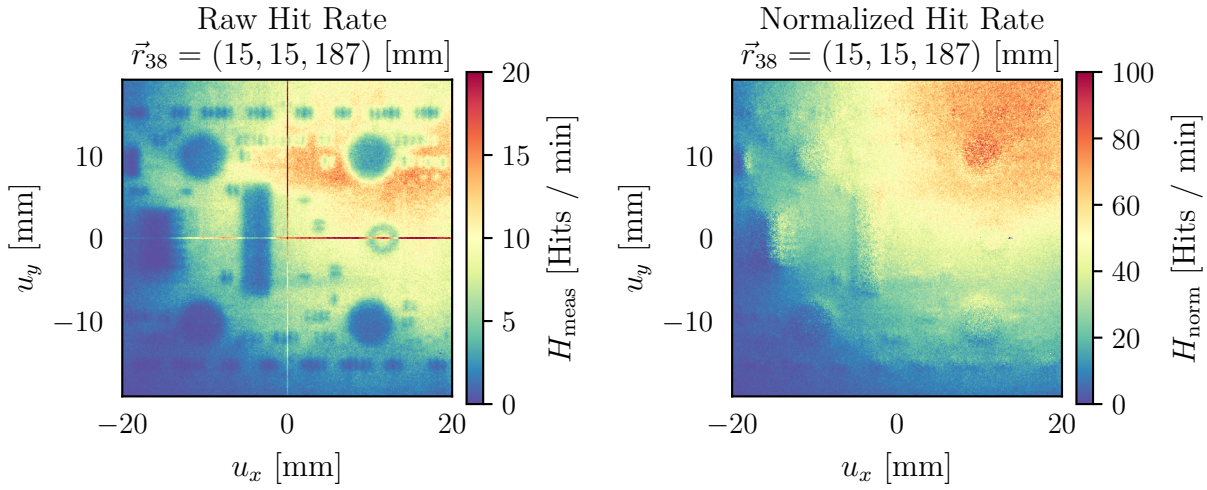

Figure 6.7.: Comparison of the raw measured hit rate for one of the source scans (left) and the normalised hit rate (right) of the same scan. The raw measured hit rate shows local patterns due to absorption from SMD components, while the normalised hit rate does not.

6.4. Source Profile & Position

Reducing test times is an effective way to increase the throughput of the QC Setup. Increasing the intensity of the radiation on the module will reduce the required time needed for the source scan. Choosing the optimal distance between the radioactive source and the module being tested is therefore a useful measure to increase the throughput.

To find the optimal position of the source, one first needs a description of the expected results of a source scan for a given source position $\vec{r}$. The expected hit rate is determined by two functions: The Spatial Intensity Profile $I_{\text{src}}(\vec{r})$ of the radioactive source and Effective Sensitivity Map $\eta(\vec{u})$ of the module's pixel at the position $\vec{u}$ in the local coordinate space of the module. The Effective Sensitivity is caused by the absorption from the SMD components above the sensor on the flex. Using these functions, the expected hit rate is:

$$H_{exp}(\vec{r}, \vec{u}) = I_{src}\,(\vec{r} + \vec{u}) \cdot \eta(\vec{u}). \tag{6.1}$$

Both of these functions are determined by measuring the hits from self-trigger source scans $H_{\text{meas}}(\vec{r}, \vec{u})$ at varying relative positions $\vec{r}$ between the module and source. In total, 43 self-trigger source scans are performed at three different heights, with each scan being $t_{scan} = 15\,\text{min}$ long.

Due to the large number of different source positions, the assumption can be made that each pixel on the module should have received approximately the same amount of radiation over all measurements. Summing over all hits across all the measurements for a given

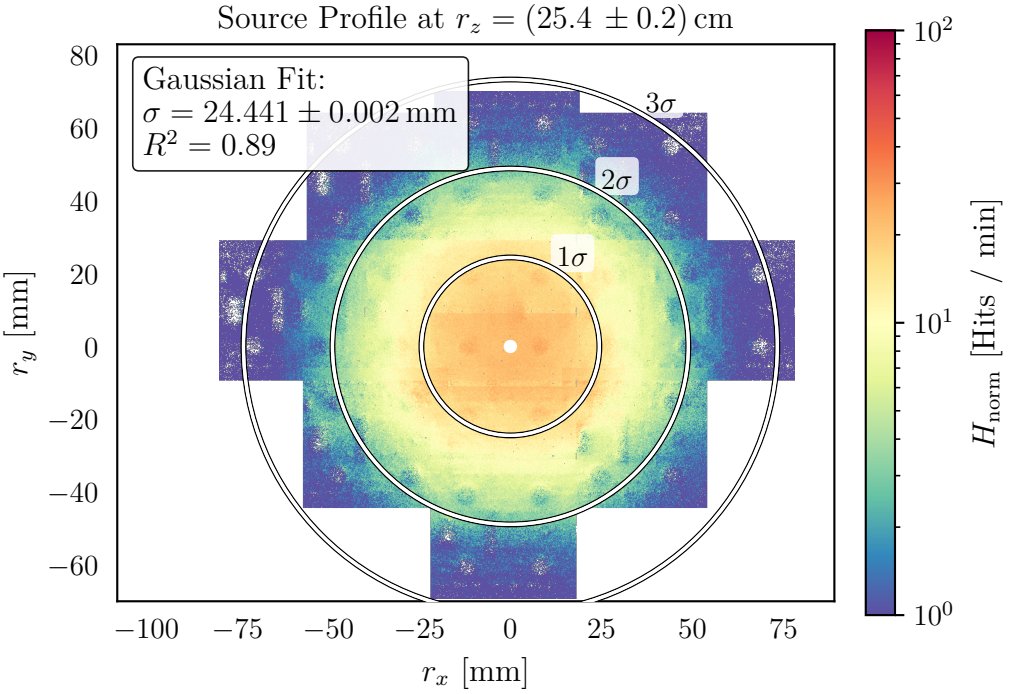

Figure 6.8.: Combination of all H_{norm} measurements for one height stitched together, resulting in an image of the intensity profile of the source.

pixel will therefore give a measure of $\eta_{\text{mod}}(\vec{u})$.

Using $\eta_{\text{mod}}(\vec{u})$, a pixelwise normalisation with $H_{\text{norm}}(\vec{u}, \vec{r}) = H_{\text{meas}}(\vec{u}, \vec{r})/\eta(\vec{u})$ is performed, resulting in maps which describe the approximate source profile. This can be seen in Figure 6.7. For each r_z, all normalised scans are combined into one global source profile of which an example is displayed in Figure 6.8. The full results for all heights are shown in Appendix B. The pattern appears to be radially symmetric. Assuming the profile is of a Gaussian nature, the intensity is fitted as:

$$I_{fit}(\vec{r}) = A(r_z) \cdot \exp\left(\frac{r_x^2 + r_y^2}{2(\sigma(r_z))^2}\right). \tag{6.2}$$

Plotting the radial profile of the measured values and fits results in Figure 6.9. It can be seen that the profile indeed follows a Gaussian shape, with R^2 scores of 0.76 at 35.4 cm, 0.89 at 25.4 cm and 0.94 at 18.7 cm for each height. As the height increases, the fit quality appears worse because the hit rate decreases and the signal-to-noise ratio declines. It can also be seen that, as one would expect, the distribution gets wider as the distance between the source and the module gets larger. Assuming a cone shape which originates from a point source, one would expect the profile width $\sigma(r)$ to increase linearly with the distance. The amplitude $A(r_z)$ is described such that the number of particles at each height is conserved. A small correction is added, due to the absorption of the radiation

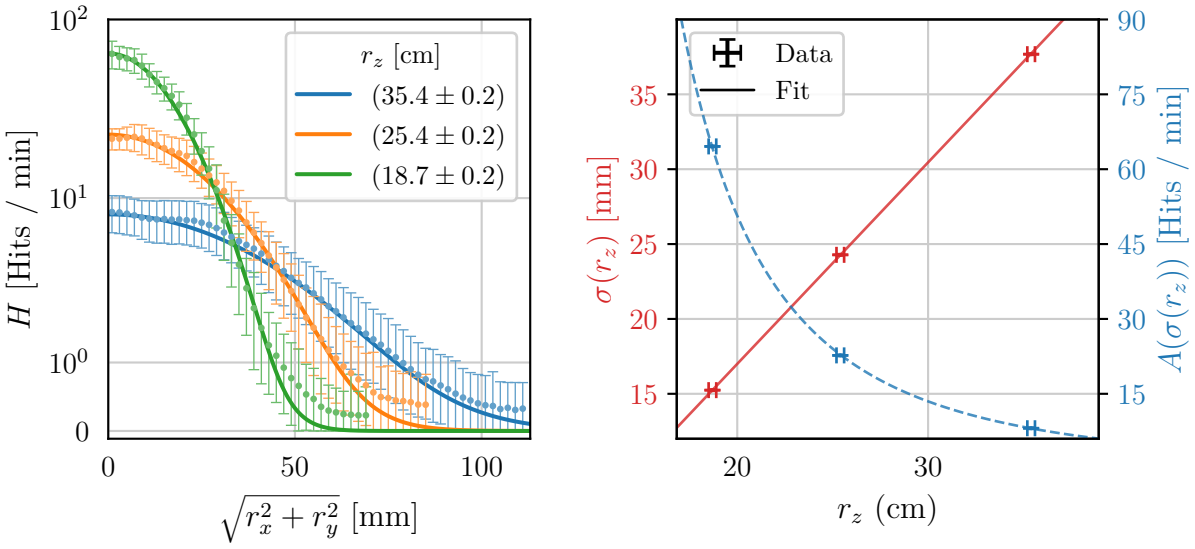

Figure 6.9.: Left: Radial shape of the measured profile and associated fits at different heights. The errorbars indicate the standard deviation of all pixels within a bin of a given radius. Right: Gaussian parameters against height assuming the profile is cone shaped (all fit parameters in appendix B).

in air:

$$\sigma(r_z) = a + b \cdot r_z, \qquad A(r_z) = \frac{A_0}{\sigma(r_z)^2} \cdot \exp\left(-k \cdot \sigma(r_z)\right). \tag{6.3}$$

The resulting maximum likelihood fit can be seen in Figure 6.9. It describes the source profile in three dimensions. Using the measured effective sensitivity $\eta_{\text{mod}}(\vec{u})$ and the source profile, the expected number of hits for any relative source position can be described using Eq. 6.1.

Placing the source too close to the module will lead to insufficient illumination of the corners and edges, while placing the module too far away loses radiation that misses the module entirely. The criterion for the optimal position $\vec{r}_{\text{opt}}$ is that the likelihood of receiving < 2 hits on any pixel is minimised for a scan of a given duration t.

$$p\left(\exists\text{pixel} : N_{\text{hit}} < n_{\text{thr}} \,\middle|\, \vec{r}, t\right) = 1 - \prod_{x,y} \left(1 - p_{\text{single}}\left(N_{\text{hit}} < n_{\text{thr}} \,\middle|\, \vec{r}, \vec{u}_{x,y}, t\right)\right) \tag{6.4}$$

The probability that an individual pixel receives $< n_{\text{thr}}$ hits is modelled via a Poisson

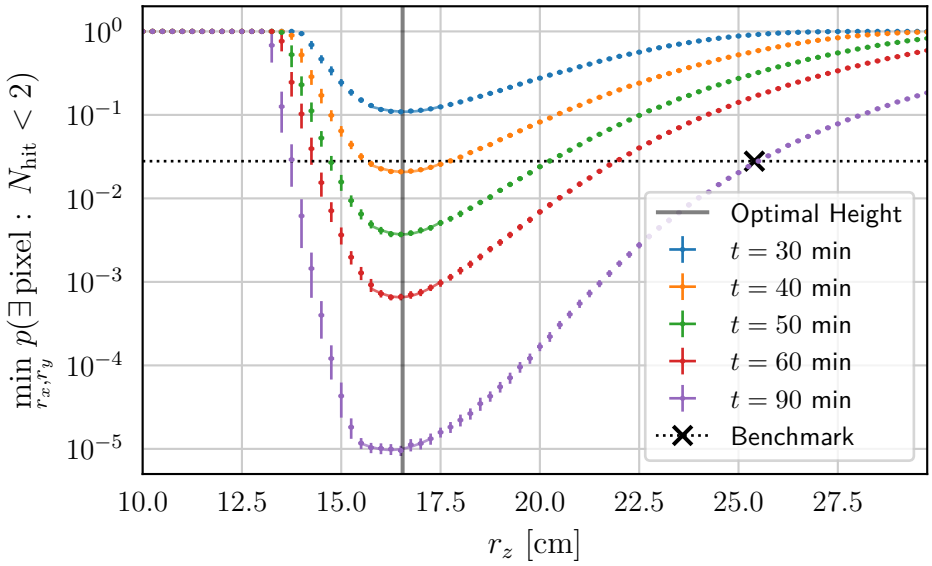

Figure 6.10.: Evaluation of different source positions along r_z at the optimal r_x, r_y position. The performance of the previous setup is indicated as a benchmark, that should be matched by the new system.

distribution with the expected value $\mu(\vec{r}, \vec{u}, t) = t \cdot H_{\text{exp}}(\vec{r}, \vec{u})$

$$p_{\text{single}}\left(N_{\text{hit}} < n_{\text{thr}} \,\middle|\, \vec{r}, \vec{u}, t\right) = \sum_{k=0}^{n_{\text{thr}}-1} e^{-\mu(\vec{r},\vec{u},t)} \frac{\mu(\vec{r}, \vec{u}, t)^k}{k!}. \tag{6.5}$$

This condition is chosen because when all good pixels receive two or more hits, one can clearly separate the dead pixels that are not sensitive to radiation and the good pixels from each other, with the one-hit bin acting as a clear separator. The resulting function against the height r_z can be seen in Figure 6.10. The optimal distance is (16.5 ± 0.1) cm. This parameter is directly used in the design of the box and this optimisation results in a reduction of the scan time by a factor of ~ 2.

6.5. Environmental Systems

As described in Section 6.1, the test chucks each need to be provided with silicone oil cooling lines, dry air supply and vacuum lines. All the supply lines are routed into the box via 3D-printed strain relief fittings on the right wall of the box, then through the front routing area of the box, through the fittings of the custom 3D-printed data adapter holder and into the chucks.

The silicone oil cooling lines are flexible PVC tubing within an insulated sleeve to prevent condensation and heat loss along the lines. The design of the cooling loop needs to

consider three major aspects: The cooling performance, operational independence of the chucks and the number of failure points. Four possible designs are considered: a parallel or serial loop, with or without independent shutoff valves. The simplest solution, a serial loop without independent shut-offs, is chosen, since it has the least number of failure points. This decision is mainly driven by significant concerns about silicone oil leaks. A slight temperature increase with each sequential chuck can be expected. In reality, this effect is not significant enough to disrupt operation. Furthermore, since there are no independent shutoffs, chucks can only be accessed while the temperature of the cooling oil is sufficiently high to prevent condensation. This operational limitation is a compromise, accepted to reduce the system's complexity and failure points.

To keep the dew point inside the chucks sufficiently low, dry air is fed into the module carriers. Regulation of this dry air is done centrally with one variable area flow meter for all chucks. To prevent the warm air from adding heat to the test chuck, the dry air is first passed through a heat exchanger connected to the silicone oil chiller and then routed together with the cooling lines inside the insulated sleeve.

The vacuum holding the modules on the test chucks is monitored independently and can be shut off independently for each chuck via the front control panel. Independent control and monitoring allow for individual placement and removal of the modules on the chucks, as well as operation with a reduced number of chucks.

6.6. Electronics and Monitoring

For each chuck, the temperature of the module, the vacuum chuck and the cold chuck, as well as the vacuum pressure, ambient temperature and humidity need to be monitored [45]. Sensor readings are digitised and processed by two independent systems: The Hardware Interlock and the DCS system, including the Software Interlock. Based on the sensor readings, the temperature of the module needs to be regulated using a Peltier element.

DCS PCB & Software Interlock The monitoring of the temperatures is performed with an *Arduino Mega 2560*. Its internal ADC has a 16-channel multiplexer, which matches the required number of incoming lines from four setups. A custom shield, shown in Figure 6.11, was created as part of this thesis. It receives all incoming connections routed through the Hardware Interlock and leaves room for four additional I2C connections. A newly created custom firmware[3] streams the data to a connected PC via

[3]Available under: https://gitlab.gwdg.de/ruben.foerster/labpy

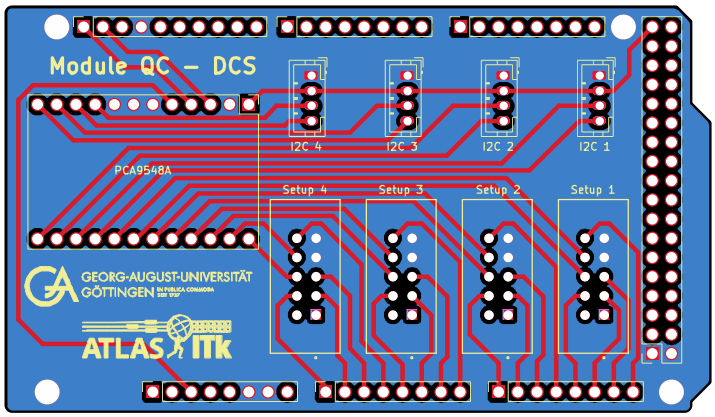

Figure 6.11.: Custom Arduino Mega Shield for the DCS system of the Source Box, including four connectors for each setup going to the Hardware Interlock PCB (right side bottom) and four I2C connectors (right side top) and a I2C multiplexer (left side).

serial. On the PC the raw ADC counts and I2C values are converted to temperatures and uploaded to a database. From there, the data can be displayed as part of a *Grafana* Dashboard. The data is also used as an input value for the Peltier control system and the Software Interlock uses it to check the condition of the setup. The Software Interlock is the primary safety system to ensure the safe operation of the module. All power and cooling commands are validated by the Software Interlock. In case unsafe conditions are reached, the Software Interlock performs corrective action and/or triggers a safe shutdown of the system by sending the appropriate commands to the power supplies.

Hardware Interlock The Hardware Interlock is a project designed in house[4]. Its main purpose is to serve as an independent safety system that triggers as a backup to the Software Interlock, in case the Software Interlock is unable to perform a safe shutdown or fails to detect a fault. In case the sensor thresholds are reached, it disconnects all power connections to the setup and stops any fault from progressing further.
It receives one ribbon cable per test setup, carrying all wires to the relevant sensors. The analogue readings are then processed by a set of operational amplifiers and the resulting voltages are read by the onboard *ATmega 2560* microcontroller or forwarded to the DCS board. All power cables to the HV, LV and Peltier elements are routed through connectors on the Hardware Interlock. If the firmware of the *ATmega 2560* determines that a threshold is reached, relays disconnect the power lines, effectively turning the setup off. This is considered an unsafe shutdown since the power is cut immediately with no

[4]Created by Dieuveil Orcel Thys-Dingou, details available under https://gitlab.cern.ch/dthysdin/interlock.

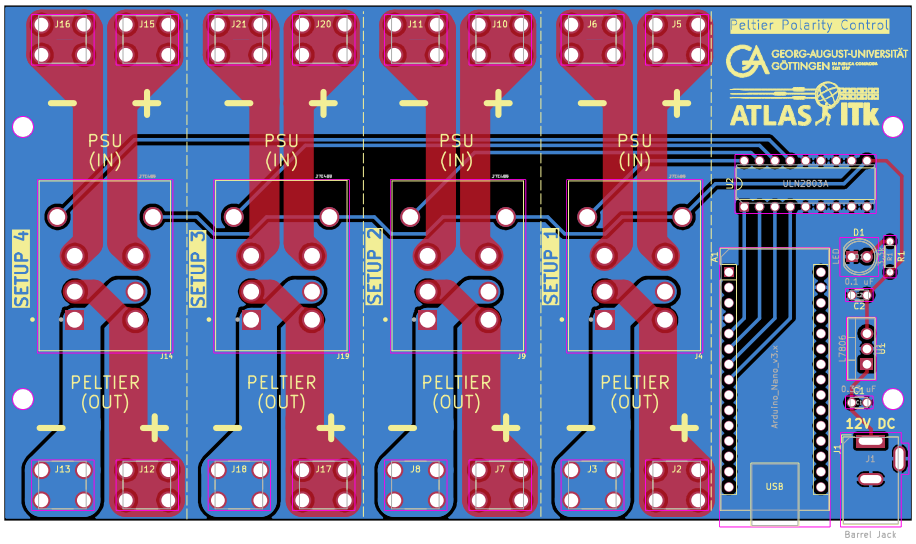

Figure 6.12.: Schematic of the custom-designed polarity-inverting PCB used for the Peltier control. Outgoing & incoming cabling is connected to the top & bottom. DPDT relays are located between the connectors. The control logic is located at the right.

ramping.

While the Hardware Interlock is completely independent of any external computer, its state can be written back to a connected PC and be shown as part of the Grafana Dashboard. The current state is also indicated via a signal light column and an audible alarm.

Peltier control To regulate the module's temperature, a PID controller is used. The temperature of the module is the controlled variable and the power supplied to the Peltier elements of the test chuck is the manipulated variable. As the employed power supplies can only provide positive voltages, a custom polarity switching PCB, developed as part of this thesis, is utilised. A schematic of this PCB can be seen in Figure 6.12. It utilises four double-pole double-throw (DPDT) relays that can be switched by sending serial commands to an Arduino Nano microcontroller. Since the 4 PID control scripts operate independently, a custom interface software communicates with the board's firmware. Incoming commands from the controllers are passed forward and return messages are matched to the correct controller and passed back.

7. Core Column Problems under Thermal Cycling

A common electrical defect encountered during the ITk production is the so-called *Core Column Problem* (CC Problem) [46]. It can manifest in multiple different ways, with symptoms often being readout issues in masking steps performed by YARR scans. This leads to repeating patterns of failing pixels in scans, such as the digital and analogue scans. An example of this can be seen in Figure 7.1. Other symptoms include complications during tuning or threshold scans. In such cases, communication issues lead to the scan freezing completely or taking much longer than expected. Issues are categorised as a CC problem when the issues can be resolved by turning one or multiple CCs off.
Since this issue cannot be observed during wafer probing but only on assembled modules, it is likely introduced during hybridisation. The hypothesis is that it is caused by physical debris introduced between the chip and sensor [46].

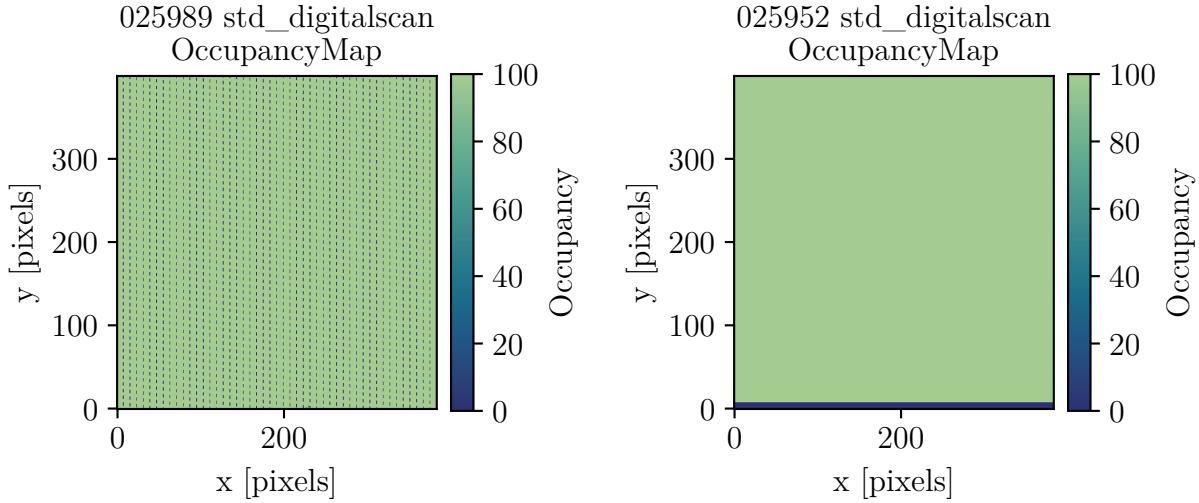

Figure 7.1.: Two Occupancy maps of digital scans from the same chip. On the left, all CCs are enabled. Readout issues lead to repeating patterns of pixels with zero hits. At the right, the bottom-most CC is disabled, with no problems in the rest of the chip.

While most CCs are discovered during the initial testing of the module, some degradation has been observed in which modules with CC issues have developed further CCs that need to be masked. Studies to understand possible causes of such degradation, therefore, need to be undertaken to ensure the number of new failures within the detector's lifetime is below an acceptable limit. One environmental factor that could lead to additional CCs problems is thermal cycling. Modules will have to survive ~ 100 temperature cycles between $-45\,°C$ and $20\,°C$ during operation [47]. A study to ensure that thermal cycling does not result in new CC problems is therefore performed.

7.1. Experimental Procedure & Setup

The thermal cycling study is performed using the thermal cycling chamber detailed in Section 5.3. Unlike during regular QC testing, thermal cycles are performed in the faster *shock* mode, due to practical reasons. The modules are moved between the $20\,°C$ warm and $-45\,°C$ cold chambers every 15 min. The induced thermal shock creates conditions which are more extreme than what is expected during operation. In total, 500 cycles are performed, going well beyond the 100 cycles expected during the detector's lifetime. Modules are held via vacuum chucks to imitate the stress acting on a module that has been cell loaded and has a carbon structure on its back side.
Electrical tests are performed at $[0, 10, 20, 50, 75, 100, 200, 500]$ cycles. To ensure this is done in a repeatable way a custom semi-automated test script is used. A flowchart displaying the logic of this script can be found in Appendix C. To keep the testing of each cycle independent, the tuning of the module and the disabled columns are reset. The script performs electrical tests, including an ADC Calibration, Analogue Readback, VCAL Calibration and Injection Capacitance tests. YARR scans with a series of different combinations of disabled CCs are performed. For each, a full series of MHT+TUN+PFA (see Section 4.6.2) is performed. The primary goal is to find the minimum number of disabled CCs needed to operate the module. Additionally, the behaviour of the CC scan (see Section 4.5) is evaluated. Disabled CCs are categorised as either *"Identified by CC Scan"* or *"Manually masked"*.

7.2. Results

Testing of two modules with the serial numbers `20UPGM23210995` (called: `0995`) and `20UPGM23211408` (called: `1408`) has been completed. The highest and lowest temperatures reached in each cycle can be seen in Figure 7.2. The average temperatures reached for

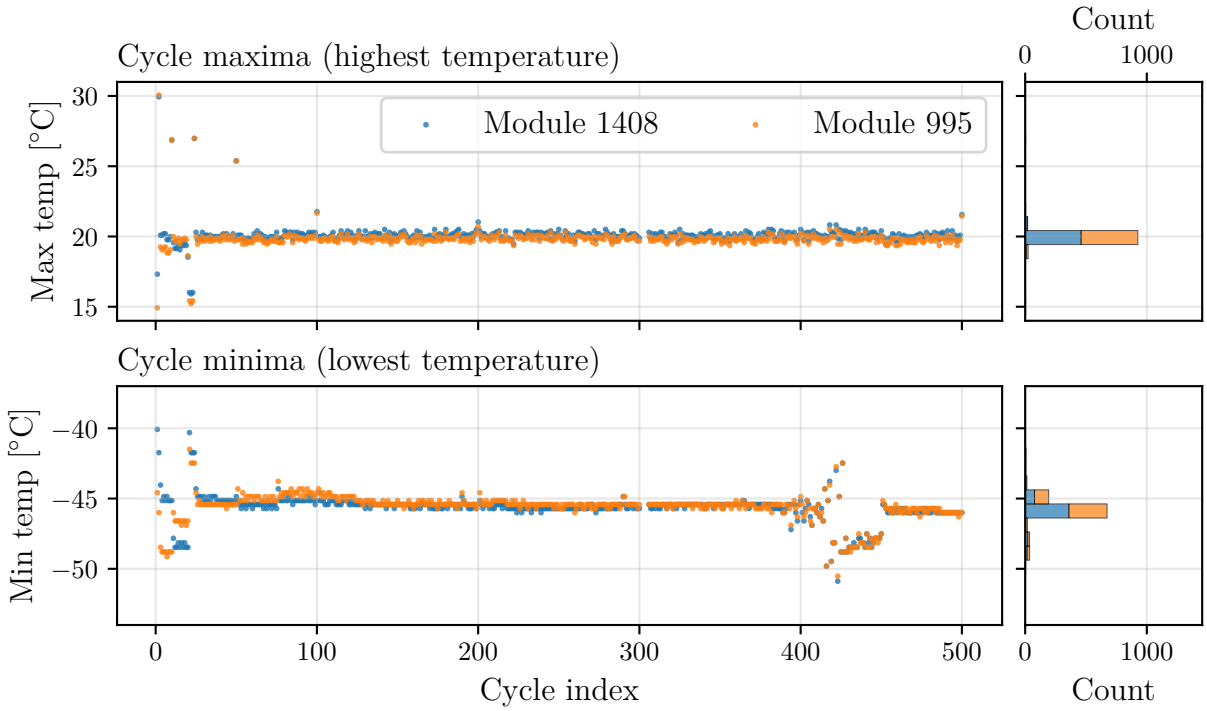

Figure 7.2.: Temperature maxima reached during thermal cycling.

both modules is $(-46 \pm 1)\,°C$ and $(20 \pm 1)\,°C$, with all cycles reaching at least $-40\,°C$ and $15\,°C$ and 98 % of cycles reaching temperatures of $< -44\,°C$ and $> 14\,°C$.

Electrical Testing

The basic electrical tests are analysed using the same tools used during production, giving relevant QC parameters at each cycling interval. Across all cycles, no clear trends or unexpected behaviour can be found. The modules pass all basic electrical tests across all cycles.

Before the cycling, 3 CCs, listed in Table 7.1, were already disabled. Two are detected by the CC scan and one is manually deactivated. Throughout the course of all cycles, no new CC failures are detected. However, the behaviour of the CC scan on Chip `0x20a5c`

Table 7.1.: Disabled CCs observed during the thermal cycling study.

Module	Chip	Column	Failed at Cycle	Type of Masking
0995	0x20a5c	1	0	CC Scan
1408	0x20a5b	33	0	CC Scan
1408	0x20a5b	35	0	Cycle 0: Manual, Cycle >10: CC Scan

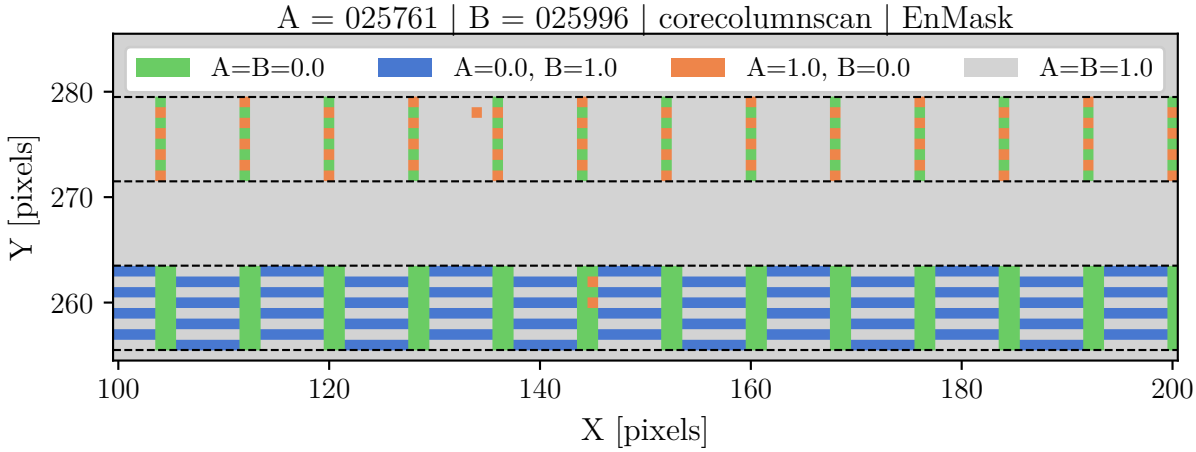

Figure 7.3.: Change in CC Scan behaviour on a section of the disabled CCs. Green indicates pixels that are masked by the CC scan both before and after cycle 10, orange indicates pixels that are only masked after cycle 10, and blue indicates pixels that are only masked before cycle 10. One can see more pixels being masked in CC 35 (top) and less in CC 33 (bottom) after cycle 10.

changes with cycle 10 and then remains this way. This can be seen in Figure 7.3. CC 35 is initially not masked by the scan, but later is masked by it, because the number of failing pixels in the column during the CC scan increases. Meanwhile, the number of failed pixels is reduced in the CC 33, but this CC is masked both before and after cycle 10 as the number of failed pixels is always sufficiently large.

Other changes in the behaviour of all scans are tracked to ensure no unexpected behaviour is seen that could precede or relate to new CC failures. No significant changes or trends related to CC issues, beyond the change in CC scan behaviour already discussed, are found.

One minor observation in a noise scan is shown in Appendix C. Since it is not repeatable and does not align with any CCs, this observation is deemed unrelated to any CC problems.

Statistical Analysis

Given the hypothesis that CC issues are caused by physical debris within that column, one can assume that only a fraction, r, of CCs are sensitive to encountering issues due to thermal cycling in the future. In the most general case, the probability of any column still working after a cycle c can therefore be modelled as

$$p_{\text{col.}}(c; r, \theta) = 1 - r + r \cdot S(c; \theta). \tag{7.1}$$

Where $S(c;\theta)$ is a function dependent on the parameters θ that describe the survival likelihood of a susceptible column after cycles c. This function must be monotonically decreasing, with $S(c=0,\theta)=1$ and $S(c\to\infty,\theta)=0$.

To evaluate the probability of a given core column surviving during the operational lifetime of the detector, one considers the failure likelihood between cycles 1 and 100. This range is chosen since modules undergo at least one cycle during their QC procedures and have to survive ~ 100 cycles during their total lifetime [47]:

$$p_{\text{col.}}(1\to 100;r,\theta) = \frac{p_{\text{col.}}(100;r,\theta)}{p_{\text{col.}}(1;r,\theta)} \tag{7.2}$$

$$= \frac{1-r+rS(100;\theta)}{1-r+rS(1;\theta)} \geq 1-r. \tag{7.3}$$

Since all columns are assumed to be independent and identical, the likelihood $\mathcal{L}_i(r,\theta)$ of encountering n_i working columns after cycling the interval between cycles c_i and c_{i-1} can be described using a binomial distribution:

$$\mathcal{L}_i(r,\theta) = \binom{n_{i-1}}{n_i} \cdot \left(\frac{p_{\text{col.}}(c_i;r,\theta)}{p_{\text{col.}}(c_{i-1};r,\theta)}\right)^{n_i} \cdot \left(\frac{p_{\text{col.}}(c_i;r,\theta)}{p_{\text{col.}}(c_{i-1};r,\theta)}\right)^{n_i-n_{i-1}}. \tag{7.4}$$

For a given set of cycling intervals, c_i, the likelihood of seeing n_i working CCs at each interval is:

$$\mathcal{L}_{\text{tot.}}(r,\theta) = \prod_{i=1} \mathcal{L}_i(r,\theta). \tag{7.5}$$

Given that no new CC issues are found after 500 cycles, one can simplify using $n_i = n_{i-1} = n_0 = 397$ to:

$$\mathcal{L}_{\text{tot.}}(r,\theta) = \left(\frac{p_{\text{col.}}(500;r,\theta)}{p_{\text{col.}}(0;r,\theta)}\right)^{n_0} \tag{7.6}$$

$$= \left(\frac{1-r+rS(500,\theta)}{1-r+rS(0,\theta)}\right)^{n_0} \tag{7.7}$$

$$= (1-r+rS(500,\theta))^{n_0} \geq C. \tag{7.8}$$

Given a confidence, C, and using Eq. 7.3, one can find a lower bound for the survival

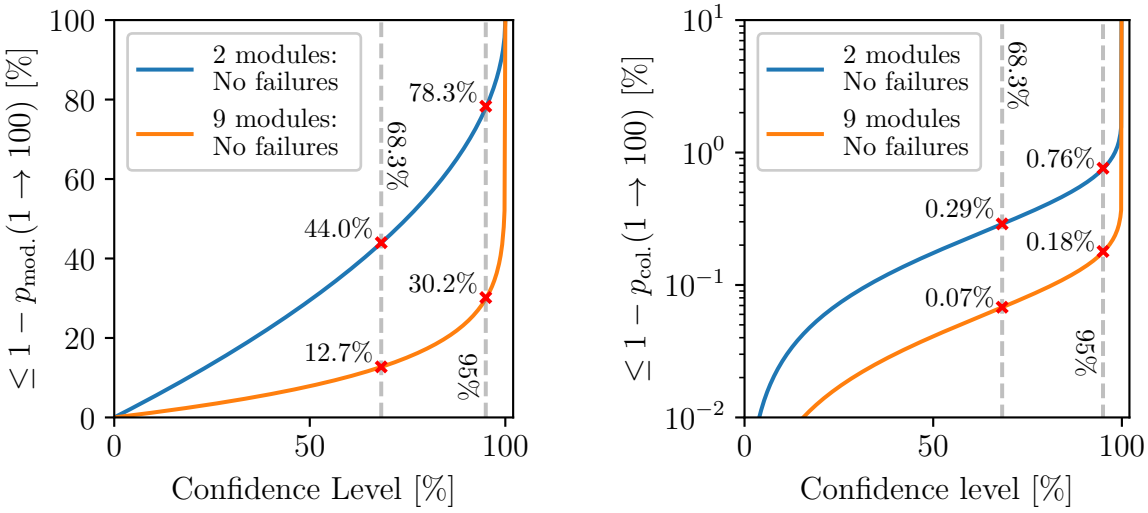

Figure 7.4.: Upper limit of the likelihood of a column failing during the operational lifetime of a module, given a confidence interval C (left) and upper limit of any given column failing during operation, given a confidence interval C (right). The upper limits for the 68.3 % and 95 % CI are highlighted in red and labeled.

probability of a column during operation as:

$$p_{\text{col.}}(1 \to 100; r, \theta) \geq (1 - r) \geq C^{1/n_0}.$$

And the probability of no column appearing on an entire module with $n_{\text{mod}} = 200$ columns is then

$$p_{\text{mod.}}(1 \to 100; r, \theta) = p_{\text{col}}(1 \to 100; r, \theta)^{n_{\text{mod}}} \geq C^{n_{\text{mod}}/n_0}. \tag{7.9}$$

This lower bound matches the case where all new failures that can occur do occur during the operation lifetime, making it also intuitively the worst-case scenario. Figure 7.4 shows the upper bound of the failure likelihood $1-p_{\text{col.}}(1 \to 100; r, \theta)$ and $1-p_{\text{mod.}}(1 \to 100; r, \theta)$ against C. One can see that with only two tested modules the 68.3 % upper limit for a CC issue appearing on a module is 44.0 % and the 95 % upper limit is 78.3 %.
Currently, 8 further modules are being tested. In the optimal case, in which no new CC issues are found, one can expect that the limits can be brought down to 12.7 % and 30.2 %, respectively. While this number gives an upper bound on the percentage of modules that might be affected, the upper bound on the ratio of columns and therefore the ratio of pixels that might need to be disabled is considerably lower at 0.29 % for the 68.3 % limit and 0.76 % for the 95 % limit.

8. Conclusion & Outlook

It has been shown that the production infrastructure in Göttingen is set up to sustain a rate of at least 20 mod/week, with many of the production steps being able to sustain rates of over 40 mod/week. The largest bottleneck is OBWBP gluing, the rate of which can be increased by either applying heat or by increasing the number of chucks used. Additionally, the availability of personnel strongly influences how efficiently the capabilities of setups can be utilised.

The construction of an electrical test stand has been completed, the setup is in operation, and numerous modules have successfully been tested in it. A picture of the finished source box is shown in Figure 8.1. The original targets of the setup have been fulfilled and the setup is well-suited for high-throughput testing of many modules with minimal training of new personnel. The radiation safety concept has been successfully validated and approved by the relevant safety department, exceeding initial requirements and allowing for an increase in up-time of the setup.

Figure 8.1.: Electrical testing setup for the ITk module production in Göttingen, constructed as part of this thesis.

All systems of the Box are designed and validated for true parallel operation of multiple modules simultaneously. To make effective use of this parallel operation, more than one YARR readout system must be used. By placing the source in an optimal position and using a lid on the chucks that absorbs less radiation, the source scan duration was reduced from 90 min to 30 min while improving the scan quality. This has a significant impact on the Box's throughput.
A limited number of challenges remain. Work is ongoing to improve the reliability of the electronics and the usage of the centrally designed cooling chucks causes significant drawbacks. Some mitigations for chuck-related issues have already been implemented. If further issues arise, one might consider replacing the chucks with a custom design. It might be recommendable to prepare such an alternative design in advance.

A standardised procedure and a semi-automated test script for studying the effects of thermal cycles on CC issues have been presented. Two modules have been cycled and no new CC issues were observed. One can find an upper bound on the probability of new CC issues appearing on a module during operation. This upper bound is 44.0 % for a 68.3 % confidence interval and 78.3 % for a 95 % confidence interval. These limits are quite large and will need to be reduced by testing more modules. This process is ongoing with 8 further modules being actively tested. The upper bound of the individual failure probability of columns is currently 0.29 % for the 68.3 % confidence interval. This value can be viewed as an upper bound on the fraction of pixels that could fail due to CC issues caused by thermal cycling during detector operation.

A. Source Box Technical Drawings

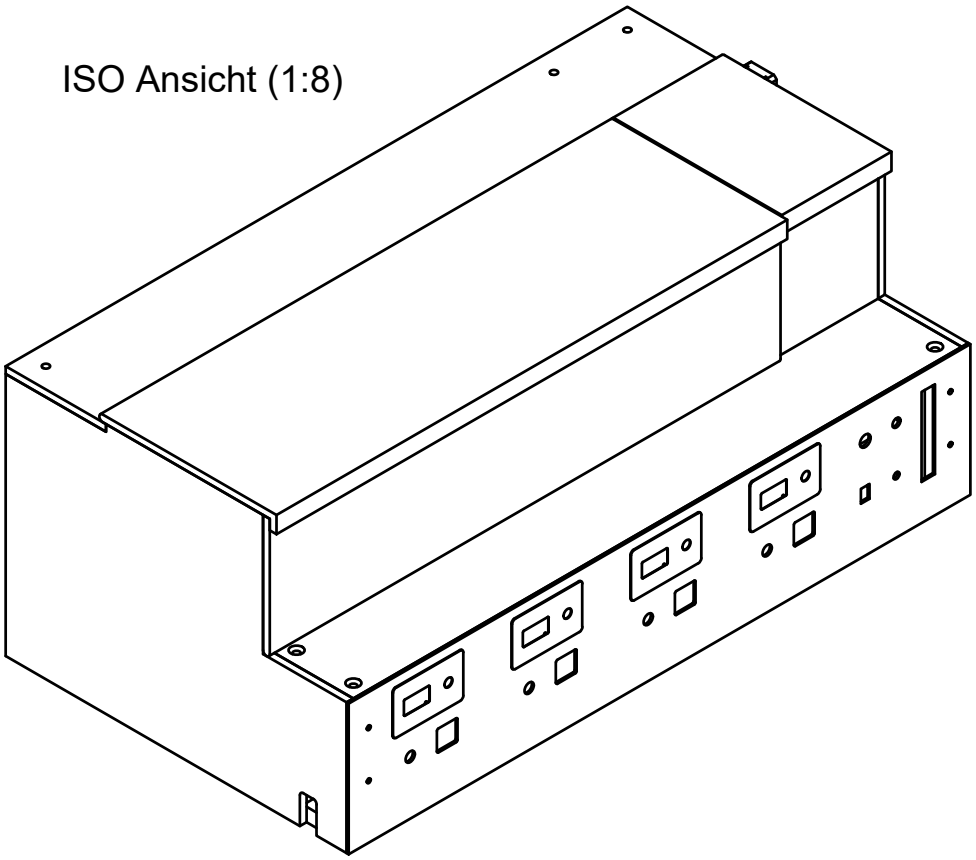

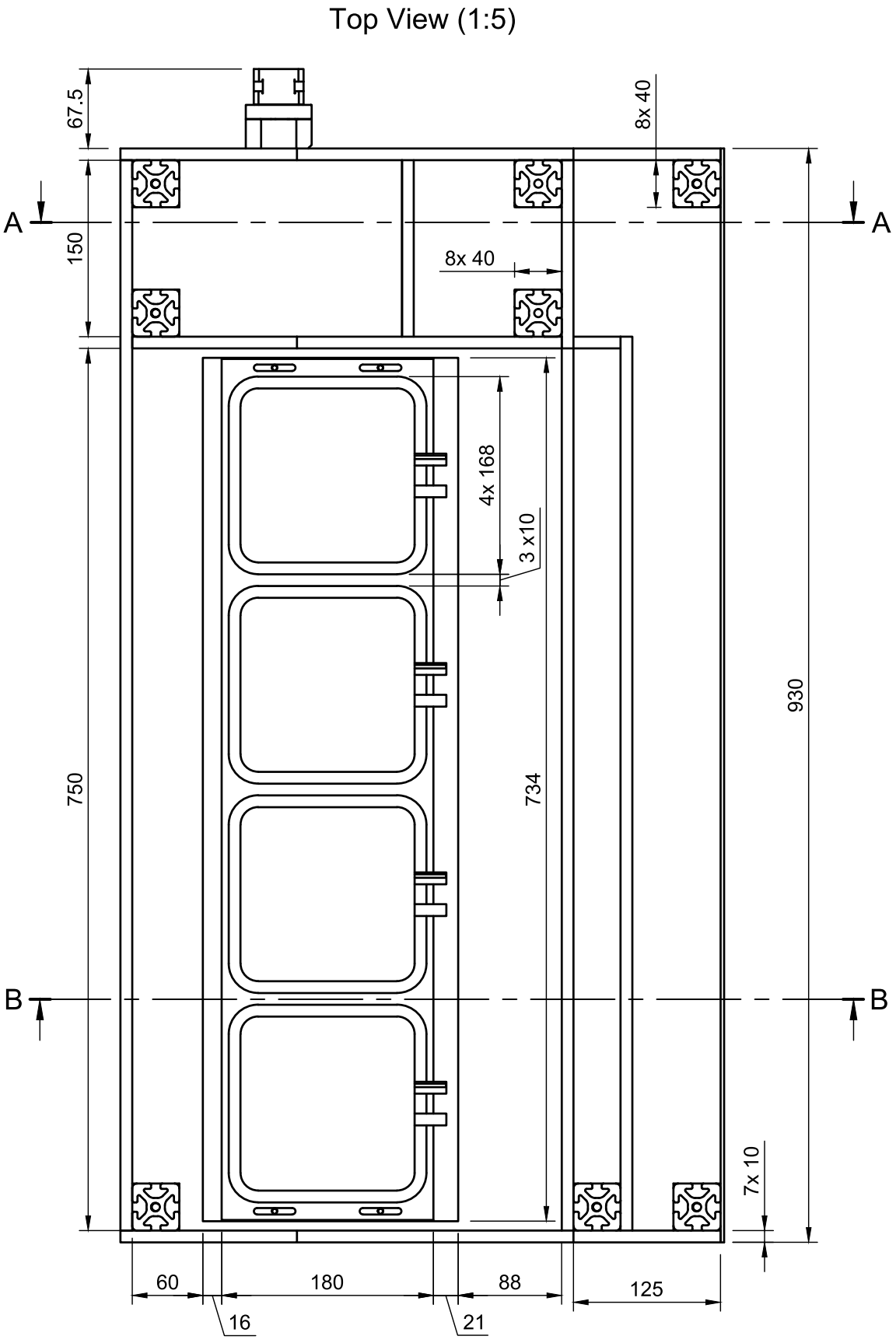
Top View (1:5)
67.5
8x 40
A
A
150
8x 40
4x 168
3 x10
930
750
734
B
B
7x 10
60
180
88
125
16
21

Right Side (1:5)

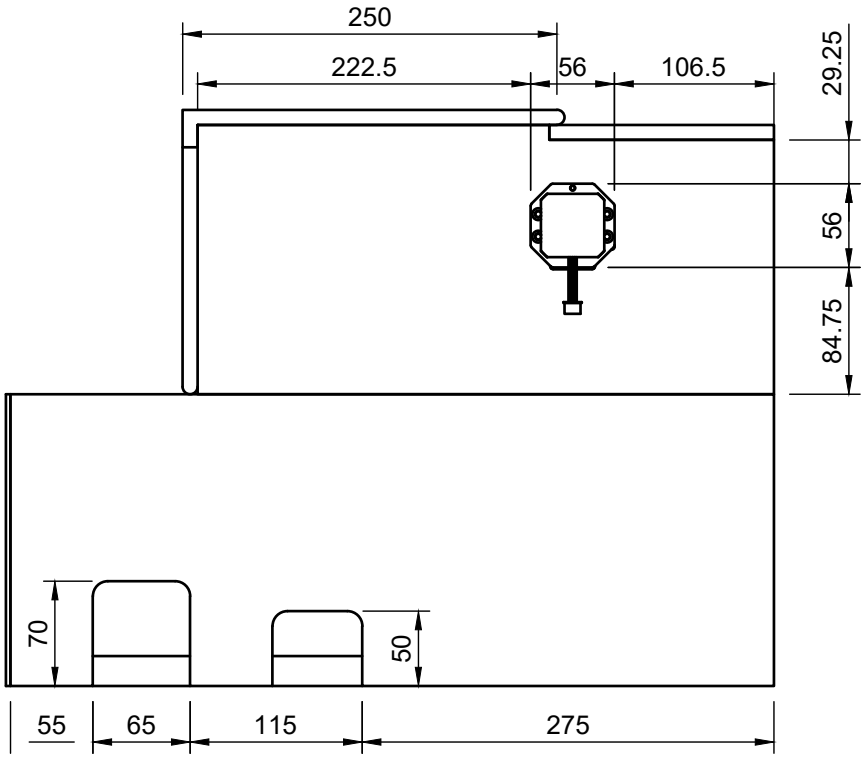

Left Side (1:5)

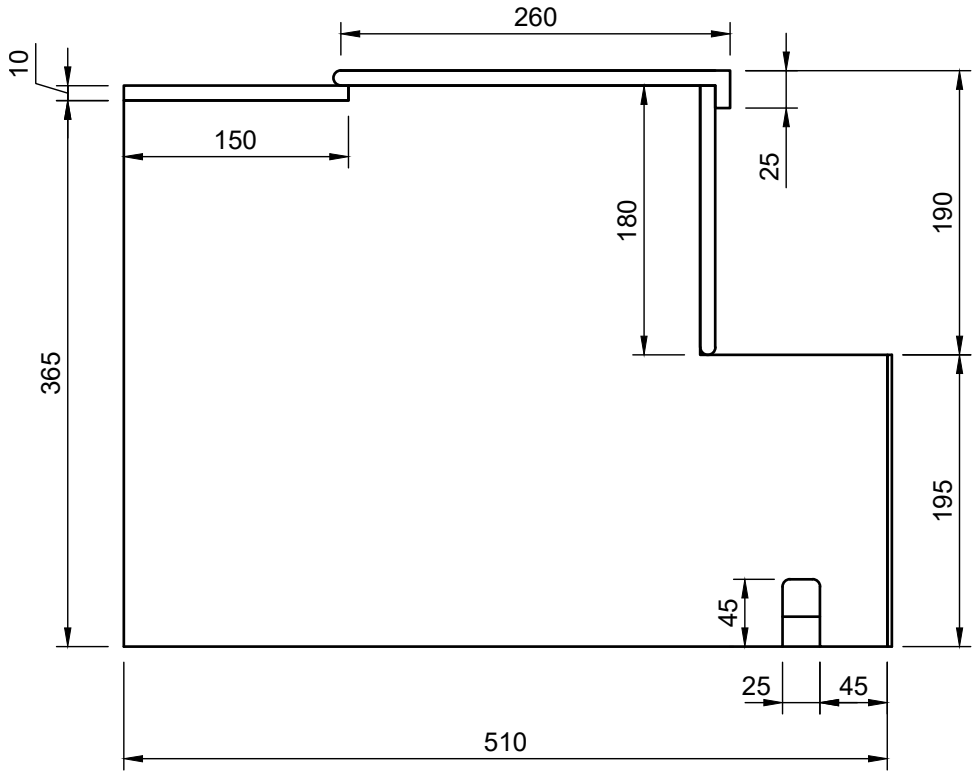

A-A (1:5)

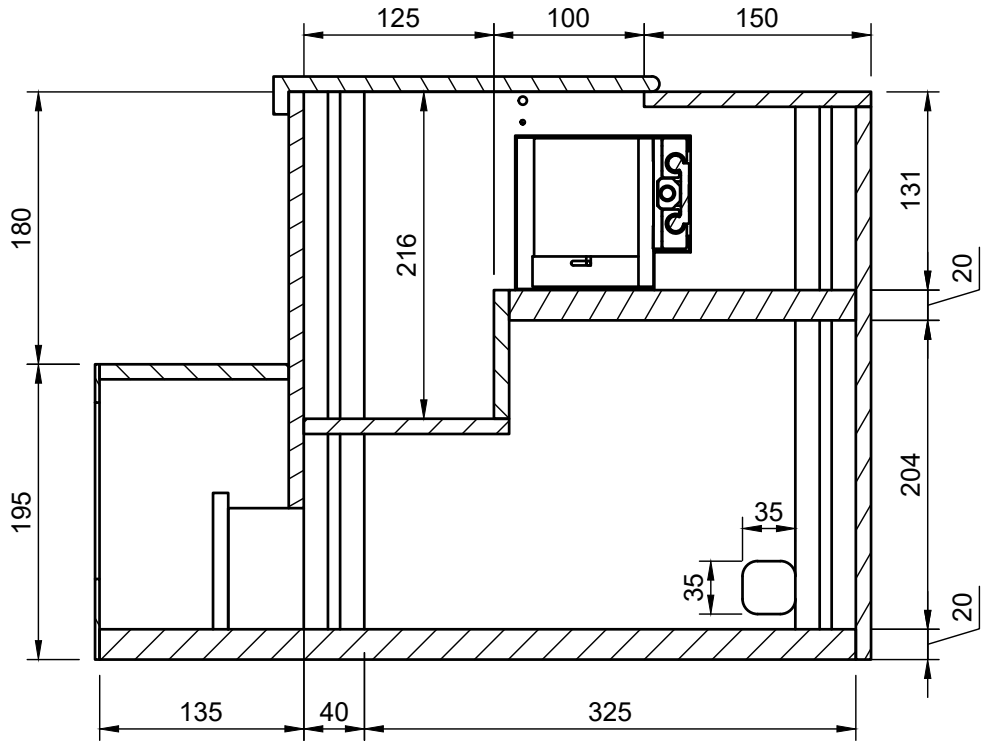
125
100
150
180
216
131
20
195
204
35
35
20
135
40
325

B-B (1:5)

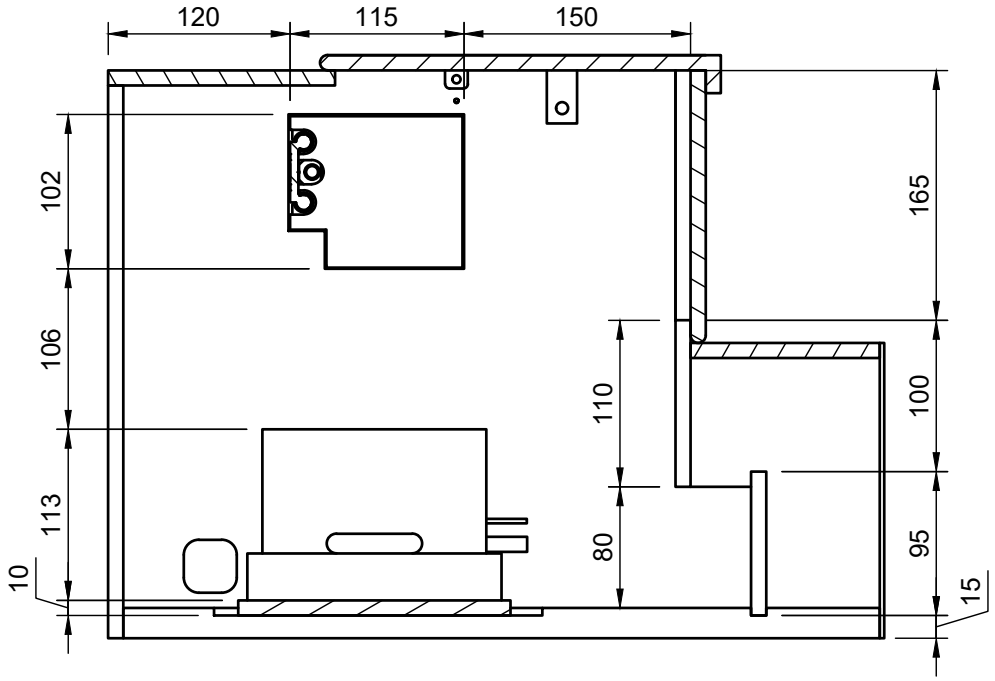
120
115
150
102
165
106
110
100
113
80
95
10
15

B. Radioactive Source Profile Measurement

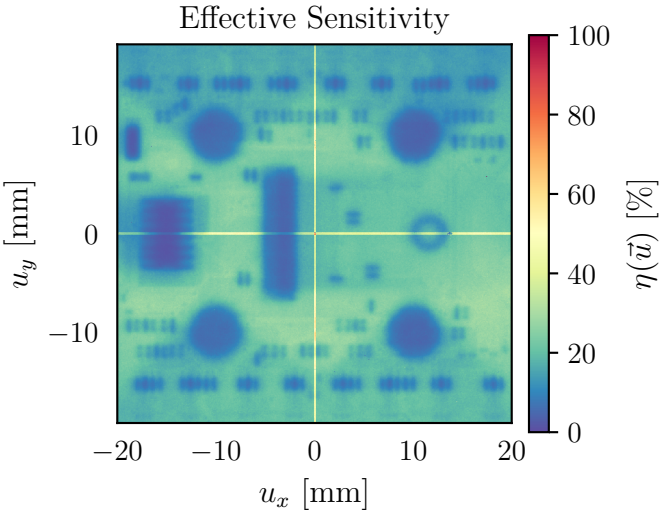

Figure B.1.: The effective sensitivity caused by absorption of SMD components on the Flex. The sensitivity is calculated by summing over all Source Scans & normalising to one. Defective pixels are disregarded. A Gaussian smoothing with $\sigma = 0.3\,\mathrm{mm}$ is applied as a means of noise reduction.

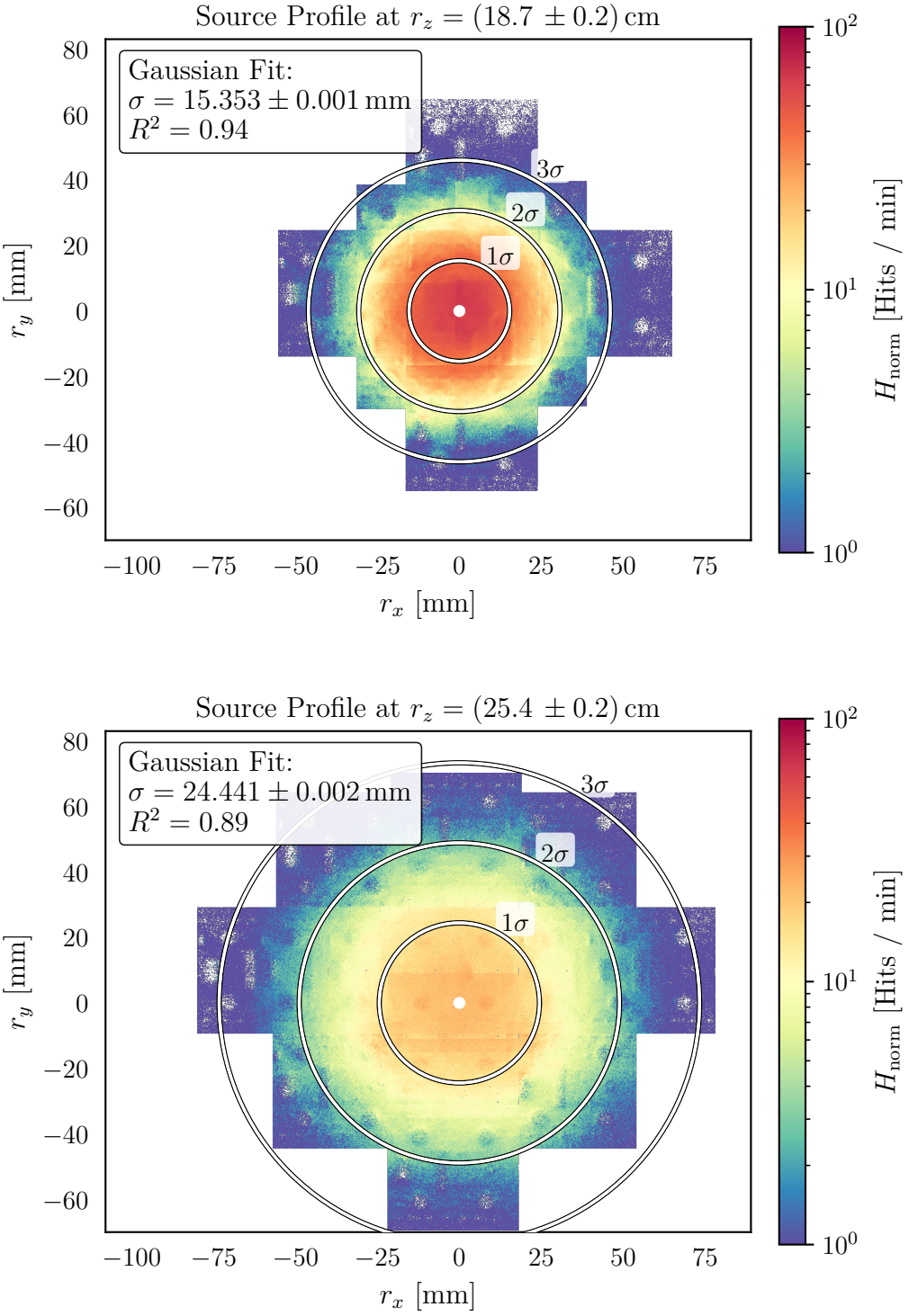
Source Profile at $r_z = (18.7 \pm 0.2)$ cm
Gaussian Fit:
$\sigma = 15.353 \pm 0.001$ mm
$R^2 = 0.94$
3σ
2σ
1σ
r_y [mm]
r_x [mm]
H_{norm} [Hits / min]
Source Profile at $r_z = (25.4 \pm 0.2)$ cm
Gaussian Fit:
$\sigma = 24.441 \pm 0.002$ mm
$R^2 = 0.89$
3σ
2σ
1σ
r_y [mm]
r_x [mm]
H_{norm} [Hits / min]

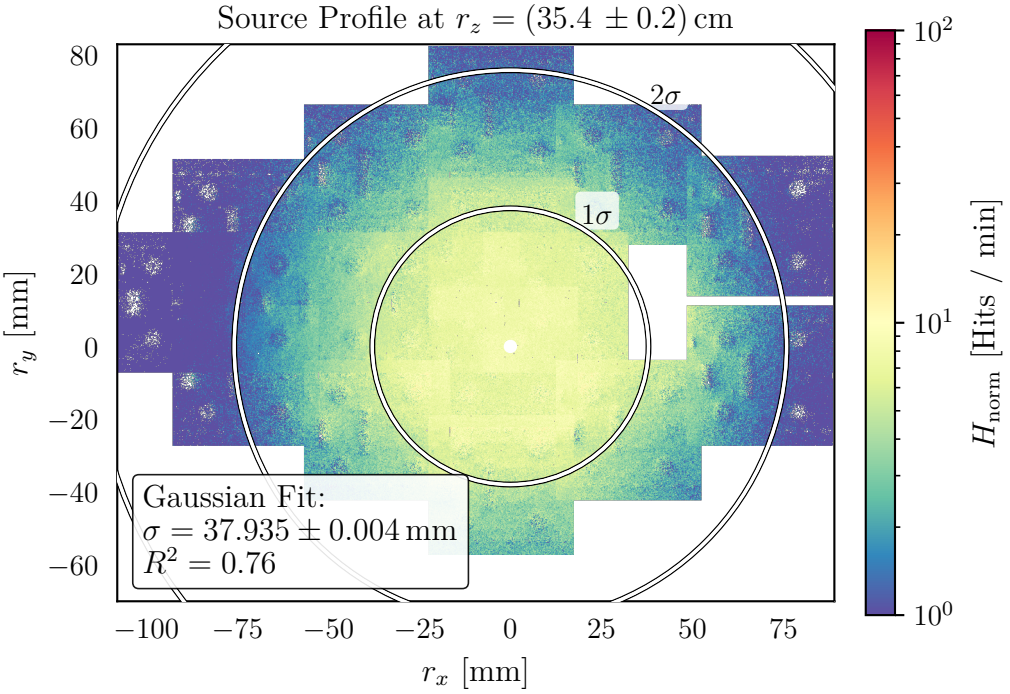

Profile Fit Parameters

Individual Gaussian Fits

Table B.1.: Gaussian fit parameters for each height.

Height [cm]	Amplitude	x_0 [mm]	y_0 [mm]	σ [mm]
18.7	64.570	−3.742	−4.306	15.244
25.4	22.699	1.936	−9.853	24.281
35.4	8.101	2.510	−11.979	37.681

Covariance Matrices

$$\text{Cov}_{18.7} = 10^{-7} \times \begin{bmatrix} 568.27 & -1.78 & -1.49 & -53.35 \\ -1.78 & 24.13 & 0.27 & -0.50 \\ -1.49 & 0.27 & 24.48 & -0.72 \\ -53.35 & -0.50 & -0.72 & 9.87 \end{bmatrix}$$

$$\text{Cov}_{25.4} = 10^{-7} \times \begin{bmatrix} 55.53 & 0.27 & -1.88 & -26.86 \\ 0.27 & 55.08 & -0.17 & 0.32 \\ -1.88 & -0.17 & 55.61 & -1.55 \\ -26.86 & 0.32 & -1.55 & 25.59 \end{bmatrix}$$

$$\mathrm{Cov}_{35.4} = 10^{-7} \times \begin{bmatrix} 10.90 & -0.60 & -0.74 & -27.17 \\ -0.60 & 253.26 & 1.33 & 39.74 \\ -0.74 & 1.33 & 327.41 & -36.24 \\ -27.17 & 39.74 & -36.24 & 149.29 \end{bmatrix}$$

Fit: Gaussian parameters vs. Height

Sigma fit results

$$a = -9.92\,\mathrm{mm}, \qquad b = 1.346\,\mathrm{cm}^{-1}.$$

$$\mathrm{Cov}_\sigma = \begin{bmatrix} 4.09 \times 10^{-3} & -1.85 \times 10^{-4} \\ -1.85 \times 10^{-4} & 8.71 \times 10^{-6} \end{bmatrix}.$$

Amplitude fit results

$$A = 17\,869.0\,\mathrm{min}^{-1}, \qquad k = 0.0117\,\mathrm{mm}^{-1}.$$

$$\mathrm{Cov}_A = \begin{bmatrix} 7.73 \times 10^{4} & 1.55 \times 10^{-1} \\ 1.55 \times 10^{-1} & 3.49 \times 10^{-7} \end{bmatrix}.$$

Optimal Source Position

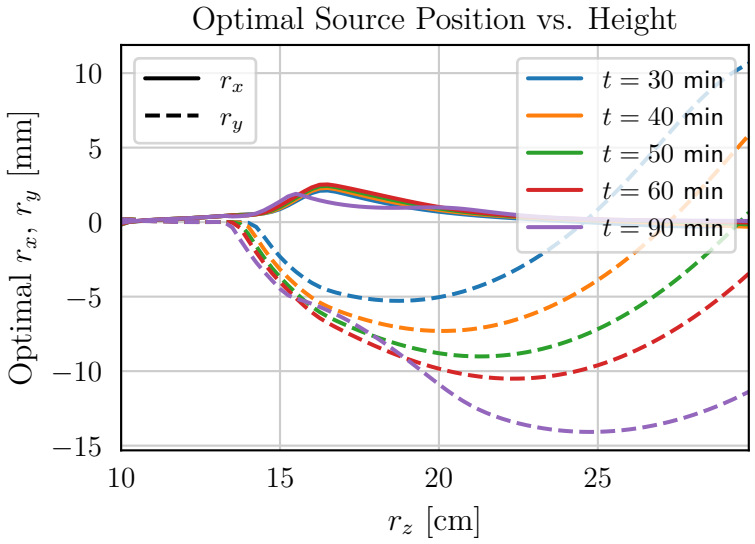

Figure B.2.: Optimal position in the horizontal plane for a given scan duration t and distance r_z (determined numerically).

C. Further Figures of Thermal Cycling Study

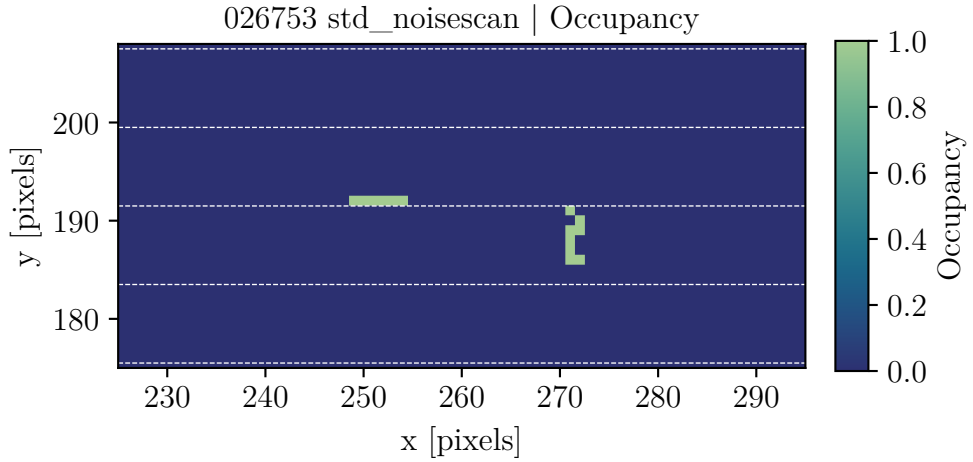

Figure C.1.: Cluster of failing pixels observed in a noise scan at cycle 500 on chip `0x20a7b`. The expected occupancy of the noise scan is zero. A pattern of 14 pixels shows an occupancy of one. This pattern is not reproducible by repeated scans with the same configuration. It does not align with any CC.

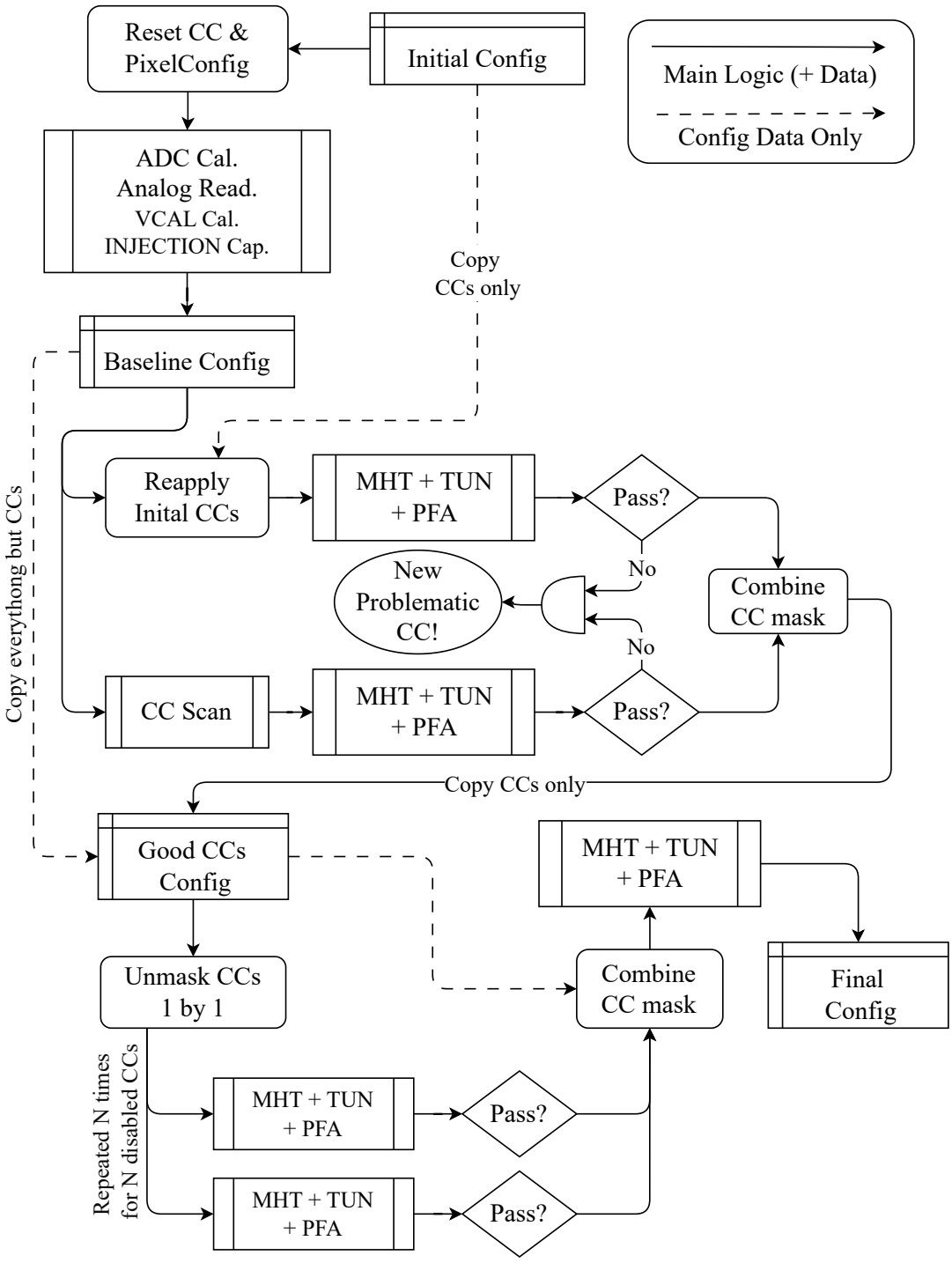

Figure C.2.: Flowchart showing a simplified logic of the testing script used at each cycling interval.

Bibliography

[1] L. Evans, P. Bryant, *LHC Machine*, JINST **3**, S08001 (2008)

[2] O. Brüning, L. Rossi, *The High Luminosity Large Hadron Collider*, World Scientific, 2nd edition (2024)

[3] ATLAS Collaboration, *Technical Design Report for the ATLAS Inner Tracker Pixel Detector*, Technical Report CERN-LHCC-2017-021, ATLAS-TDR-030, CERN, Geneva (2017)

[4] ATLAS Collaboration, *Observation of a new particle in the search for the Standard Model Higgs boson with the ATLAS detector at the LHC*, Phys. Lett. B **716**, 1 (2012)

[5] ALICE Collaboration, *The ALICE experiment at the CERN LHC*, JINST **3**, S08002 (2008)

[6] LHCb Collaboration, *The LHCb Detector at the LHC*, JINST **3**, S08005 (2008)

[7] ATLAS Collaboration, *The ATLAS Experiment at the CERN Large Hadron Collider*, JINST **3**, S08003 (2008)

[8] CMS Collaboration, *The CMS experiment at the CERN LHC*, JINST **3**, S08004 (2008)

[9] ATLAS Collaboration, *ATLAS Insertable B-Layer Technical Design Report*, Technical Design Report CERN-LHCC-2010-013, ATLAS-TDR-019, CERN, Geneva (2010)

[10] ATLAS Collaboration, *ATLAS Pixel Detector Electronics and Sensors*, JINST **3**, P07007 (2008)

[11] A. Ahmad, et al., *The silicon microstrip sensors of the ATLAS semiconductor tracker*, Nucl. Instrum. Meth. A **578**, 98 (2007)

[12] B. Mindur (ATLAS), *ATLAS Transition Radiation Tracker (TRT): Straw tubes for tracking and particle identification at the Large Hadron Collider*, Nucl. Instrum. Meth. A **845**, 257 (2017)

[13] ATLAS Collaboration, *ATLAS Muon Spectrometer*, Technical Design Report CERN-LHCC-97-022, CERN, Geneva (1997)

[14] ATLAS Collaboration, *ATLAS Magnet System*, Technical Design Report CERN-LHCC-97-018, CERN, Geneva (1997)

[15] M. Thomson, *Modern Particle Physics*, Cambridge Univ. Press (2013)

[16] ATLAS Collaboration, *Technical Design Report for the Phase-II Upgrade of the ATLAS TDAQ System*, Technical Report CERN-LHCC-2017-020; ATLAS-TDR-029, CERN, Geneva (2017)

[17] H. Kolanoski, N. Wermes, *Particle Detectors: Fundamentals and Applications*, Oxford Univ. Press, Oxford (2020)

[18] A. Einstein, *Über einen die Erzeugung und Verwandlung des Lichtes betreffenden heuristischen Gesichtspunkt*, Annalen Phys. **322(6)**, 132 (1905)

[19] A. H. Compton, *A Quantum Theory of the Scattering of X-rays by Light Elements*, Phys. Rev. **21**, 483 (1923)

[20] H. Bethe, *Theory of the Passage of Fast Corpuscular Rays Through Matter*, Annalen Phys. **5**, 325 (1930)

[21] J. Townsend, *The conductivity produced in gases by the motion of negatively-charged ions*, Nature **62(1606)**, 340 (1900)

[22] C.-C. Sun, T.-X. Lee, *Optical Design for LED Solid-State Lighting*, IOP Publishing, Bristol, UK (2022)

[23] W. Shockley, *Electrons and Holes in Semiconductors*, Van Nostrand, New York (1950)

[24] A. L. Heggelund, et al., *Overview of the ATLAS ITk pixel detector*, JINST **18(02)**, C02014 (2023)

[25] ATLAS Collaboration, *Technical Design Report for the ATLAS Inner Tracker Strip Detector*, Technical Report CERN-LHCC-2017-005; ATLAS-TDR-025, CERN, Geneva (2017)

[26] Y. Tian, et al., *ATLAS ITk Pixel Pre-production Planar Sensor Characterisation for the HL-LHC Upgrade*, PoS **Pixel2022**, 067 (2023)

[27] D. A. Giugni, *Pixel Quad Module Assembly DWG*, Engineering Drawing, CERN Internal (2025), AT2-IP-ED-0010, v. 11, EDMS

[28] R. L. Bates, *Technical Specification for ITk Pixel Modules*, Specification Document, CERN Internal (2022), AT2-IP-ES-0009, v. 3, EDMS

[29] M. Garcia-Sciveres (RD53collaboration), *RD53C Chip Manual*, Technical Report CERN-RD53-PUB-24-001, CERN, Geneva (2024)

[30] J. Kampkötter, et al., *Characterization and verification of the Shunt-LDO regulator and its protection circuits for serial powering of the ATLAS and CMS pixel detectors*, J. Phys. Conf. Ser. **2374(1)**, 012071 (2022)

[31] K. E. Metcalfe, *Wire Bond Protection (OB) Assembly and QC Procedures*, Procedure Document, CERN Internal (2021), AT2-IP-AP-0005, v. 1, EDMS

[32] Y. Tian, *Final Steps Towards Production of the ITk Pixel Detector for the ATLAS High-Luminosity Upgrade*, Ph.D. thesis, Univ. Göttingen (2025), CERN-THESIS-2024-378; II.Physik-UniGö-Diss-2024/02

[33] T. Fritzsch, et al., *Experience in fabrication of multichip-modules for the ATLAS pixel detector*, Nucl. Instrum. Meth. A **565**, 309 (2006), proc. Int. Workshop on Semiconductor Pixel Detectors for Particles and Imaging

[34] J. E. Metcalfe, *Parylene Coating and Masking Procedures*, Procedure Document, CERN Internal (2021), AT2-IP-AP-0002, v. 1, Draft for comments, EDMS

[35] D. A. Giugni, *Araldite 2021*, Note, CERN Internal (2021), AT2-IP-AN-0004, v. 1, EDMS

[36] R. L. Bates, *Quad Module Carrier*, Engineering Drawing, CERN Internal (2023), AT2-IP-ED-0018, v. 3, EDMS

[37] D. A. Feito, *Design Overview of the Loaded Local Supports for the ITk Pixel Outer Barrel*, Engineering Report, CERN Internal (2023), AT2-IP-ER-0046, v. 1, EDMS

[38] T. Heim, *YARR - A PCIe based readout concept for current and future ATLAS Pixel modules*, J. Phys. Conf. Ser. **898(3)**, 032053 (2017)

[39] R. L. Bates, *Digital Module Tests*, Quality Assurance Plan, CERN Internal (2022), AT2-IP-QA-0025, v. 1, EDMS

[40] R. L. Bates, *Production Flow and QA/QC of Modules*, Quality Assurance Plan, CERN Internal (2021), AT2-IP-QA-0011, v. 1, EDMS

[41] L. Selem (ATLAS), *ATLAS ITk Production Database use and tools for the ITk Pixels community*, JINST **20(06)**, C06029 (2025)

[42] R. L. Bates, *OB WBP item and attachment SQ procedures*, Quality Assurance Plan, CERN Internal (2022), AT2-IP-QA-0022, v. 1, EDMS

[43] C. Gemme, *Module Yield Task Force Report*, Engineering Report, CERN Internal (to be published) (2025), AT2-IP-ER-0111, v. 1, EDMS

[44] L. Teich, *Quality Control of Modules in the ATLAS Inner Tracker*, Bachelor's thesis (2025), II.Physik-UniGö-BSc-2025-02

[45] R. L. Bates, *Testing set-up SQ procedures*, Quality Assurance Plan, CERN Internal (2020), AT2-IP-QA-0022, v. 1, EDMS

[46] C. Hultquist (ATLAS), *The "Core Column" Issue in ATLAS ITk Pixel Modules* (2025), ATL-ITK-SLIDE-2025-696, CDS

[47] J. Grosse-Knetter (ATLAS ITK), *ATLAS ITk Pixel Module Bump Bond Stress Analysis*, PoS **Pixel2022**, 056 (2023)

Acknowledgements

I would like to thank Arnulf Quadt and Jörn Große-Knetter for giving me the opportunity to work as part of the ITk production and for trusting me to help support the production in Göttingen. I especially want to thank Jörn for always answering my day-to-day questions and listening to me talking endlessly.
I would like to thank the members of the central mechanical workshop for helping me with their expertise in the design of the source box and for undertaking the construction of the box. I would like to thank Orcel Thys-Dingou and Ali Skaf for their help with electronics for the source box. I also want to thank the student helpers working as part of the ITk production for their help with much of the labour involved in performing many of the presented production steps and measurements.
For helping me proofread this thesis, I want to thank Niklas Grün, Leander Teich and Steffen Korn. Additionally, I want to thank Steffen for advising me on the statistical analysis performed in this thesis.
Thank you to all the members of the second institute for welcoming me into the group and having many fun discussions at CaPhy break and I especially want to thank Paolo and Leander for being awesome office mates. And last but not least I want to thank my family and friends and especially my girlfriend Stella for having my back during this time, even when I would spend way too much time at the lab.

Erklärung zur Nutzung von ChatGPT und vergleichbaren Werkzeugen im Rahmen von Prüfungen

In der hier vorliegenden Arbeit habe ich ChatGPT oder eine andere KI wie folgt genutzt:

- ❑ gar nicht
- ❑ bei der Ideenfindung
- ❑ bei der Erstellung der Gliederung
- ❑ zum Erstellen einzelner Passagen, insgesamt im Umfang von _____% am gesamten Text
- ☒ zur Entwicklung von Software-Quelltexten
- ☒ zur Optimierung oder Umstrukturierung von Software-Quelltexten
- ☒ zum Korrekturlesen oder Optimieren
- ❑ Weiteres, nämlich: _____

Ich versichere, alle Nutzungen vollständig angegeben zu haben. Fehlende oder fehlerhafte Angaben werden als Täuschungsversuch gewertet.

_____

Ruben Förster
January 30, 2026

Erklärung nach §17(9) der Prüfungsordnung für den Bachelor-Studiengang Physik und den Master-Studiengang Physik an der Universität Göttingen:

Hiermit erkläre ich, dass ich diese Abschlussarbeit selbständig verfasst habe, keine anderen als die angegebenen Quellen und Hilfsmittel benutzt habe und alle Stellen, die wörtlich oder sinngemäß aus veröffentlichten Schriften entnommen wurden, als solche kenntlich gemacht habe.

Darüberhinaus erkläre ich, dass diese Abschlussarbeit nicht, auch nicht auszugsweise, im Rahmen einer nichtbestandenen Prüfung an dieser oder einer anderen Hochschule eingereicht wurde.

Göttingen, den January 30, 2026

(Ruben Förster)